A Framework for Scalable Part-scale Laser Powder Bed Fusion Simulation

by

Xin Liu

A dissertation submitted in partial fulfillment of
the requirements for the degree of

Doctor of Philosophy

(Mechanical Engineering)

at the

UNIVERSITY OF WISCONSIN–MADISON

2024

Date of final oral examination: 08/16/2024

The dissertation is approved by the following members of the Final Oral Committee:

Frank Pfefferkorn, Professor, Mechanical Engineering
Vadim Shapiro, Professor, Emeritus Mechanical Engineering
Krishnan Suresh, Professor, Mechanical Engineering
Lianyi Chen, Associate Professor, Materials Science and Engineering
Shiva Rudraraju, Associate Professor, Mechanical Engineering

A FRAMEWORK FOR SCALABLE PART-SCALE LASER POWDER BED FUSION SIMULATION

Xin Liu

Under the supervision of Professor Frank Pfefferkorn

At the University of Wisconsin-Madison

The objective of this research is to build a thermomechanical simulation framework for the Laser Powder Bed Fusion (LPBF) process which is capable of capturing the effect of scanning path for part-scale problems. Additive Manufacturing (AM) has revolutionized the production of complex components across various industries. As one kind of AM technique, LPBF is a method that enables the fabrication of intricate metal parts layer by layer using a high-energy laser beam to selectively melt and fuse metal powder. While the LPBF process holds immense promise for advancing manufacturing capabilities, the optimization of process parameters and the prediction of final part quality remain significant challenges due to the complex thermal history. The complex thermal history directly influences the microstructure, mechanical properties, and overall performance of the final part. Simulation of the thermal history and the residual stress is a critical step toward understanding these complexities. However, the conventional simulation approach is computationally expensive and not applicable to the part-scale problem. In this thesis, I proposed a thermomechanical simulation framework for the laser powder bed fusion process. The proposed framework includes the thermal and mechanical simulation approach on multiple scales and their synergistic integration. On the path level, I developed a

scalable PBF thermal history simulation which is validated by melt pool images. I validated the simulation against melt pool images captured with the co-axial melt pool monitoring (MPM) system on the NIST Additive Manufacturing Metrology Testbed (AMMT). Based on the path-scale thermal history, I developed a framework for simulating the LPBF process residual stress. I developed this framework by introducing a new concept termed effective thermal strain to capture the anisotropic thermal strain near and around the melt pool. I validated my approach with the high-fidelity results from the literature. I developed a layer-level thermal simulation approach that considers the laser scanning paths. I further synergistically integrated the path-level and layer-level methodologies. The proposed simulation framework provides efficient path-level thermomechanical simulation results, predicting the melt pool length with only a 10% relative error compared to experimental data. Compared with existing approaches, the path-level simulation requires only 1/45 of the number of discretized elements to simulate the same problem as studied in the literature. This integration further enables efficient access to the path-level thermal history within complex part-scale 3D structures. This research offers a simulation framework that enhances the predictive capabilities for LPBF on the part scale, which is crucial to applications such as the design and optimization of process parameters for improved part quality. This approach exploits the highly localized nature of the LPBF process. Quantifying these localized characteristics remains a work in the future, which can help develop better simulation tools.

ACKNOWLEDGMENTS

I would like to express my deepest gratitude to my advisor, Professor Frank Pfefferkorn, for his support, guidance, and encouragement in my research and the writing of this thesis. His support and expertise has been invaluable, and without his direction, this thesis would never have been written. I would also like to thank Professor Vadim Shapiro for his expertise and guidance, which have added considerably to my graduate research experience. His rigorous approach to research has been enlightening. Without his guidance and support, this research would not have been possible.

I am also grateful to the members of my thesis committee, Professor Krishnan Suresh, Professor Lianyi Chen, and Professor Shiva Rudraraju, for their constructive comments and suggestions, which have greatly improved the quality of my work.

Special thanks to my collaborator, Xingchen Liu, for his valuable contributions and assistance in various aspects of this research. I would also like to thank my collaborators, Neel Goldy Kumar and Hongrui Chen, for their discussions and time in our collaborative work. Additionally, I would like to acknowledge Intact Solutions, Inc. for providing a stimulating research environment and access to necessary resources.

I am thankful to my peers and colleagues, Randi Wang, Yaqi Zhang, Vaidyanathan Thiagarajan, Parag Pathak, for their friendship, support, and the numerous discussions that have enriched my understanding and experience during my studies.

My heartfelt appreciation goes to my parents for their unwavering support and encouragement throughout my academic journey. Their patience and belief in me have been a constant source of motivation. Lastly, I would like to express my profound gratitude to my girl friend, Li Zhao, for her encouragement and support, without

which I would not have been able to persevere through the challenges of my PhD journey.

Thank you all for your support and encouragement.

CONTENTS

LIST OF TABLES

LIST OF FIGURES

NOMENCLATURE

h	Convection coefficient
k	Conductivity
T	Temperature
T_m	Melting temperature
α	Absorptivity
P	Laser power
V	Laser speed
H_i	Laser input energy on element i
ϵ_e	Elastic strain
ϵ_t	Thermal strain
ϵ_p	Plastic strain
ϵ_{total}	Total strain
σ_x	Cauchy stress normal component in x direction
σ_y	Cauchy stress normal component in y direction
σ_z	Cauchy stress normal component in z direction

1 INTRODUCTION

1.1 Motivation

Additive Manufacturing (AM) has revolutionized the production of complex components across various industries [4]. One of the most promising AM techniques is Laser Powder Bed Fusion (LPBF), a method that enables the fabrication of intricate metal parts layer by layer using a high-energy laser beam to selectively melt and fuse metal powder [5, 6, 7, 8]. The LPBF process begins with a 3D model of the part to be manufactured, which is sliced into thin layers along the building direction. In each layer, metal powder is first spread as a thin layer. Then, the laser moves according to a predefined scanning path to melt and solidify the powder, forming the desired cross-section. After each layer is built, the build platform lowers, and a new layer of powder is spread. This process repeats until the part is complete. LPBF can utilize various metal powders, such as stainless steel [9], Inconel alloys [10], and titanium alloys [11]. The process's use of thin layer thickness and small hatch distance (as shown in Figure 1.1) allows for the production of intricate geometries. This capability to produce lightweight yet strong structures makes LPBF advantageous in many industries, including aerospace [12], automotive [13], and healthcare [14].

While the LPBF process holds immense promise for advancing manufacturing capabilities, the optimization of process parameters and the prediction of final part quality remain significant challenges due to the complex thermal history and high computational cost simulate the thermomechanical process. The complex thermal history directly influences the microstructure [15], mechanical properties [16, 17],

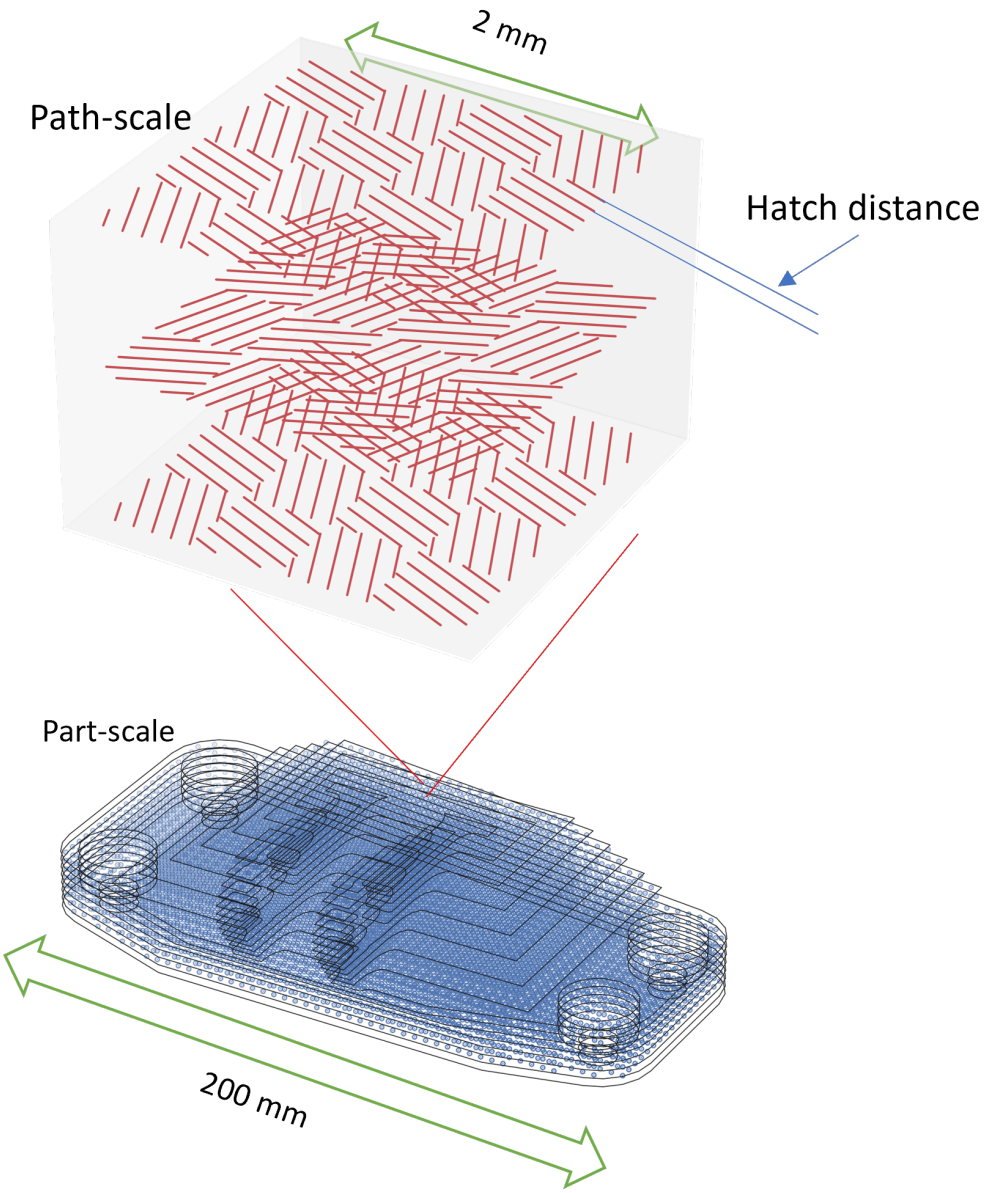

Figure 1.1: Schematic: the scales of LPBF process.

and overall performance of the final part. The localized heating and rapid cooling inherent in the LPBF process introduce complexities that necessitate a nuanced understanding of the process dynamics. The laser scanning path is one of the major factor which contributes to these complexities. Simulation is critical to capture these complexities [18].

Currently, conventional simulation approaches for LPBF are either too computationally expensive for practical use or too inaccurate to capture the process's complexities. These conventional methods require fine spatial discretization and small time steps to accurately model the moving melt pool, making them impractical due to their high computational costs. Practical part-scale approaches often ignore the temperature dependence of materials or adopt a layer-based approach, simplifying the simulation process into a sequence of layer activation and solidification rather than following the actual scanning path. While layer-based approaches are much faster, they fail to account for the complexities introduced by the scanning path. Some other studies use analytical or semi-analytical approaches [19, 20]. These approaches are efficient, but they ignore the temperature dependence of the material properties, which might also cause inaccuracy in some circumstances.

The LPBF process indeed has some characteristics which could be exploited for better simulation. Specifically, the LPBF process involves highly localized thermomechanical evolution. The input laser energy quickly dissipates as the distance from the laser center increases. Materials exhibit lower stiffness at higher temperatures, leading to a higher tendency for plastic deformation. Due to the commonly used constant laser power and speed, the melt pool during the process tends to have a

consistent profile. Existing approaches have noted these characteristics and attempted to exploit them, but there is a lack of a systematic formulation to fully utilize them.

1.2 Proposed work

I will outline a multiscale thermomechanical simulation framework for the laser powder bed fusion process. The proposed framework synergistically integrate the path-scale approach and the part-scale approach, make the simulation efficient while able to capture the effect of scanning path. The idea is to establish a framework which knows when to use which approach, and how the results from different approaches can be exchanged. Specifically, when approaching to the critical regions, the simulation need to switch from lower fidelity approaches to the higher fidelity approaches, see Figure 1.2. The proposed framework consists of the major steps as listed below:

1. The path-level LPBF thermal simulation. I developed a scalable PBF thermal history simulation based on melt pool physics and dynamics. Different from the existing approaches, the new simulation approach uses a Voronoi diagram based on the scanning path, making its discretization is conducted on the scanning path and covers the entire simulation domain to consider all powders and solid. The new approach also uses a modified conduction model that considers the high thermal gradient around the melt pool.

2. The path-scale mechanical simulation. I developed a framework for simulating the LPBF process residual stress based on the path-level thermal history. I developed this framework by introducing a new concept termed effective

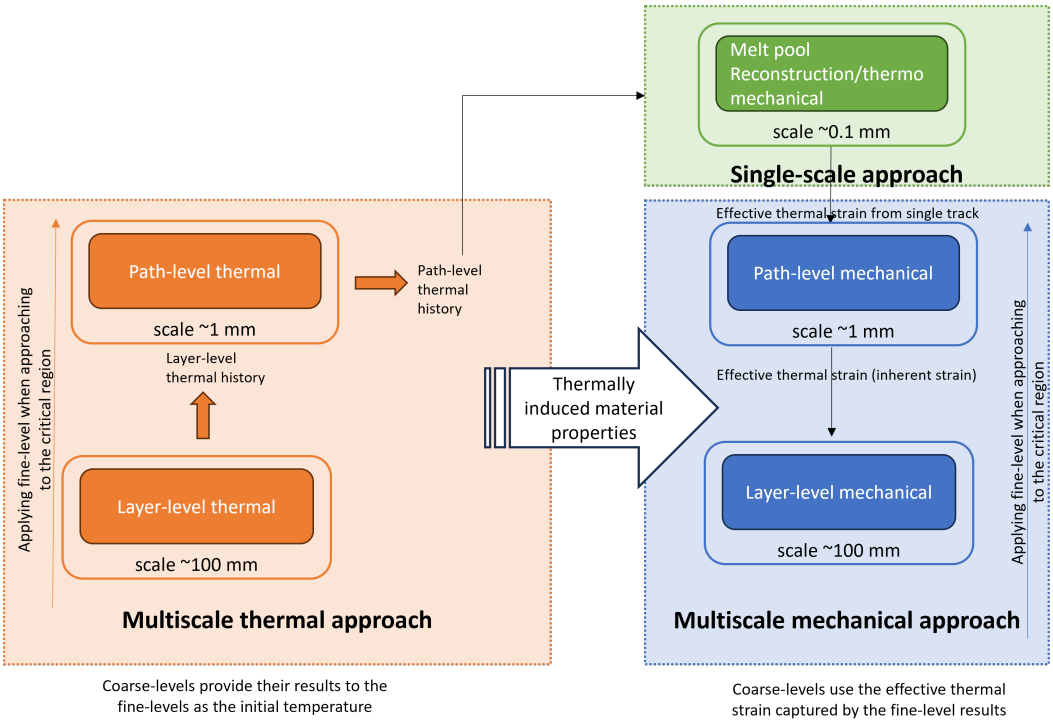

Figure 1.2: The framework of the proposed multiscale thermomechanical approach.

thermal strain to capture the anisotropic thermal strain near and around the melt pool. Compared with the existing approaches, the path-level simulation requires discretization only to capture the scanning path rather than the details of the melt pools, thus requiring less dense mesh and is more computationally efficient.

3. The Layer-level and multiscale simulation. I firstly developed a layer-level simulation which considers the scanning paths. Then I synergistically integrated both the path-level and layer-level methodologies. This integration enables efficient access to the path-level thermal history within complex 3D structures.

1.3 Outline

The remainder of this thesis is organized as follows[1]. In Chapter 2, I will discuss the state of the art in LPBF simulation approaches, classifying them based on spatial scale. Researchers have developed the microscale simulation approach, which considers multiphysics and multiphase interactions. The voxel-based approach, a simplification of the microscale simulation, has also been proposed. Due to the inefficiency of the voxel-based approach, other researchers have introduced the layer-based approach. While the layer-based approach is applicable to part-scale engineering problems, it fails to consider the effects of the scanning path, leading to inaccuracies.

Chapter 3 discusses the proposed path-level thermal simulation. In this chapter, I will first introduce the current issues in LPBF thermal simulation. Then, I will present the formulation of our path-level thermal simulation, followed by its validation. The validation dataset and measurement methods will be discussed. Next, I will compare the simulation results with experimental data, including the melt pool length and width, and provide an analysis of the results. Lastly, I will summarize this approach, its applications, and potential future work. I will also introduce a modified absorptivity model that could further improve the accuracy of the approach. Additionally, I will briefly present a collaborative work that uses path-scale thermal history to reconstruct the melt pool shape, which is an important step in path-level mechanical simulation.

Chapter 4 discusses the proposed path-level mechanical simulation. In this chapter, I will first introduce the current issues in LPBF mechanical simulation. Then, I will

[1]This dissertation is written so that each chapter is self-contained

present the formulation of the path-scale mechanical simulation framework. Four major steps will be discussed: (a) reconstructing the melt pool on a fine scale, (b) obtaining the path-scale thermal history, (c) computing the effective thermal strain, and (d) applying the effective thermal strain in the path-scale mechanical simulation. Next, I will compare the results of the proposed approach with those from different approaches in the literature. Additionally, I will demonstrate the results of the new approach on various checkerboard patterns and shapes consisting of multiple islands. Lastly, I will discuss the results and their implications.

Chapter 5 discusses the proposed layer-level simulation and the hybrid approach. In this chapter, I will first present the current issues in layer-level LPBF thermal simulation. Then, I will outline the formulation of my approaches: a layer-level approach and a hybrid layer-path approach. I will compare our results with the experimental results of a 3D overhang structure built by NIST. Next, I will analyze our results and discuss how the overhang affects the time duration over different temperature thresholds and how the thermal history evolves layer by layer.

I will summarize the contributions of this thesis and discuss extensions and open issues in Chapter 6.

2.1 Microscale simulation

Simulating the Laser Powder Bed Fusion (LPBF) process is a complex multiphysics and multiphase problem when all the different physical phenomena and interactions between phases are modeled. For instance, simulating melt pool dynamics might involve various factors such as solidified metal powders [21], the fluid dynamics of molten metal flow [22], the particle dynamics of metal powders [23], and the gas dynamics of evaporated metal gas [24]. All these factors interact with each other [25], making the simulation highly intricate. Such detailed simulations have been conducted and have provided valuable insights into the LPBF process [25]. However, microscale simulations require high-fidelity modeling of multiple physics phenomena, including powder dynamics, fluid dynamics of molten metal, and interactions between molten metals and metal powders. The extremely high computational cost makes it impractical to use these simulations for practical applications. These approaches are often limited to very short printing paths. For example, it can take up to 4000 minutes to simulate a single scan melt pool within a $390 \times 210 \times 50 \mu m^3$ domain [26]. To simulate LPBF residual stress, researchers have made various assumptions to simplify the models. For instance, the liquid or gas phase is often replaced by an equivalent solid volume or is completely ignored [27].

2.2 Voxel-based approach

To reduce the computational burden, researchers simply the microscale simulation as a thermomechanical problem on solid. I will refer it as voxel-based approach in this thesis. This approach uses fine voxel discretization to capture the melt pool shape, modeling all materials—including powders, melted metals, and solid metals—as a bulk material.

The voxel-based simulation is based on multiple assumptions and techniques which are used to simplify the modeling. Firstly, the fluid flow upon melting is not explicitly modeled [28]. All materials, including powder, liquid, and solid materials, are represented as a continuum with modified material. The material is modeled by some material properties such as density, Young's modulus, and Poisson ratio. These material properties are modeled as functions of temperature. Under this assumption, modeling of grain structure, powder spatial configuration, and liquid melt pool are no longer needed. Many papers have been published on simulating the melt pool shape using these assumptions, often with fine spatial and temporal discretization [2, 29, 30].

Weak coupling between thermal and mechanical simulation is a common assumption used in voxel-based approach. This assumption is based on the observation that the deformation during the LPBF process is small. Specifically, it suggests the mechanical analysis relies on the thermal analysis but the thermal analysis is independent of the mechanical analysis [29]. Therefore, I only need to consider the temperature changes that drive thermal expansion/shrinkage in the mechanical analysis. This assumption also allows the asynchronous thermal analysis before the mechanical analysis.

In the mechanical analysis, the total strain ϵ_{total} in the LPBF process is decomposed as:

$$\boldsymbol{\epsilon_{total}} = \boldsymbol{\epsilon_t} + \boldsymbol{\epsilon_e} + \boldsymbol{\epsilon_p} \tag{2.1}$$

where $\boldsymbol{\epsilon_t} + \boldsymbol{\epsilon_e} + \boldsymbol{\epsilon_p}$ are the thermal, elastic and plastic strain, respectively. Plastic $\boldsymbol{\epsilon_p}$ is obtained with the given plastic model, for example Von-Mises yield criterion. Thermal strain is obtained with a given thermal history in the form $\boldsymbol{\epsilon_t}(T) = \epsilon_t(T)[1, 1, 1, 0, 0, 0]^T$, where

$$\epsilon_t(T) = \int_{T_m}^{T} \alpha(t)dt \tag{2.2}$$

The thermal expansion coefficient $\alpha(t)$ is a function of temperature t. Figure 2.1 shows the $\alpha(t)$ for Ti6Al4V which I used in the present work. The reference temperature T_m is the metal melting point. All strain and stress states will be reset to zero when the temperature is above the melting point. The vector $[1, 1, 1, 0, 0, 0]^T$ indicates the thermal strain is isotropic in the normal directions x, y, z (the first three ones) and zero shear strain (the last three zeros). Despite employing isotropic thermal strain, the voxel-based approach has the capability to capture anisotropic stress with sufficient fine discretization. With adequate resolution, this approach can effectively capture the sequence of melting and solidification of the elements. The stress experienced by an element can vary depending on whether it is surrounded by already solidified elements or not. This variation can be reflected by the thermal gradient near the melt pool.

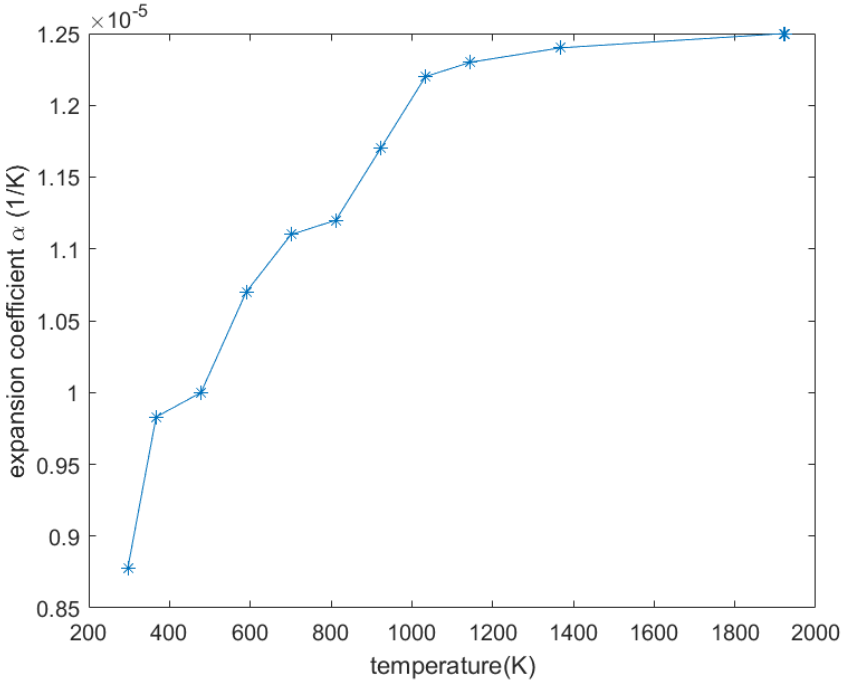

Figure 2.1: The expansion coefficient of Ti6Al4V as a function of temperature.

A technique called element birth and death is frequently used in simulating the LPBF process [31]. This technique simulates the powder deposition process in the LPBF process. The powder deposition process is a layer-by-layer process. In each layer, the laser moves according to the scanning path to melt and solidify the metal powders. The direct modeling of this process is computationally expensive. Assuming the deformation during the scanning process is small, the element birth and death technique avoids such direct modeling by initializing and meshing the entire domain and updating the stiffness matrix of the mesh to mimic the deposition process. All elements are initially assigned a material property that is considered approximately void. This property will be switched to the normal value when powders are deposited

in the layer to simulate the powder deposition process. For example, the element's Young's modulus may be initially assigned a very small value, such as 10^{-4} of the normal value [32, 33]. It will be switched to the powder's effective bulk material properties when powder deposition occurs on the element.

Based on the above assumptions, the stepwise quasi-static mechanical simulation uses the equation below:

$$\boldsymbol{\nabla\sigma} = 0 \tag{2.3}$$

$$\boldsymbol{\sigma} = \boldsymbol{C\epsilon_e} \tag{2.4}$$

$$\frac{\partial \boldsymbol{u}}{\partial \boldsymbol{r}} = \boldsymbol{\epsilon_{total}} = \boldsymbol{\epsilon_t} + \boldsymbol{\epsilon_e} + \boldsymbol{\epsilon_p} \tag{2.5}$$

$$\boldsymbol{\epsilon_t}(T) = \int_{T_m}^{T} \alpha(t)dt[1,1,1,0,0,0]^T \tag{2.6}$$

The plastic strain $\boldsymbol{\epsilon_p}$ is computed with the plasticity model. In the present work, I use the Von Mises yield surface. $\boldsymbol{u}, \boldsymbol{r}$ are the displacement and the coordinates respectively. The thermal strain is an integration of the thermal history T according to the equation above. The thermal history T comes from the thermal simulation which is a transient analysis driven by the moving heat source. The mechanical analysis is a step-wise quasi-static analysis. In each step, the mechanical analysis can take the corresponding thermal history from the thermal analysis. The laser energy input is typically modeled as a Gaussian [34] or ring [35] distribution, with the center moving along the predetermined scanning path.

Many studies have used the finite element method (FEM) to implement this formulation [36, 37, 30]. The effects of different scanning strategies in the LPBF

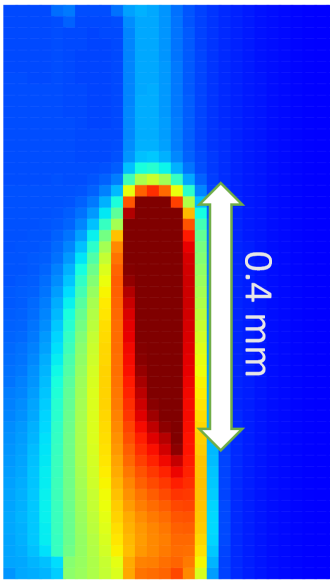

Figure 2.2: A melt pool temperature snapshot obtained by finite element method.

process have been investigated in several papers [38, 39, 40]. Figure 2.2 shows an example of the melt pool temperature snapshot simulated this method.

Though voxel-based thermomechanical simulations have a reduced cost compared to microscale simulations, they are still computationally expensive and limited to relatively short and simple scanning paths [29]. This is because the discretization must be fine enough to capture the details of the melt pool. Since the melt pool size is small (typically around 100 μm in width for a typical LPBF process), the elements from the discretization need to be smaller (usually on the order of 10 μm). A small time step (usually on the order of microseconds) is needed because the time step must be compatible with the element size to ensure numerical stability. The small time step and element size make the computational cost of thermal-mechanical simulations prohibitively high for large-part simulations. Consequently, a naive implementation

of FEM remains computationally expensive because it requires not only small time steps to resolve the high cooling rate (more than $100°C/s$) [15], but also high spatial resolution to capture the large size difference between melt pools (100 μm) and printed parts (10-100 mm). For example, simulating a 2 mm × 2 mm three-layer structure may take up to 10 hours[30]. Simulating a single layer of the same size can take more than one day[41]. This inefficiency is primarily due to the need for small element sizes around the melt pool and small time steps. The voxel-based approach scales with the fourth power of the element size: it necessitates three orders of refinement spatially for 3D space and one order temporally.

2.3 Layer-based approach

One of the main reasons for the high computational cost of conventional thermo-mechanical simulations in modeling the LPBF process is the need for dense spatial discretization and small time steps. To address this issue, agglomeration methods have been proposed. These methods use an intermediate, agglomerated model that is much larger than the scale of the spatial discretization elements, significantly reducing the computational cost. One common agglomerated model is the "superlayer"[42], an artificial layer composed of multiple adjacent real powder layers. Layer-wise approaches, such as the flash heating method[43, 44, 45, 46] and the inherent strain method [47, 48, 49], have been proposed to improve efficiency. In these methods, the scanning path is no longer considered; instead, the superlayers are activated in sequence. Due to fewer steps and less dense meshes, these methods are significantly more efficient than conventional thermal-mechanical simulations. However, by disre-

garding the scanning path, these approaches lack the capability to predict the effects of scanning paths.

For thermal simulation, researchers developed the flash heating method [46, 45]. In this approach, the moving heat source is replaced by an equivalent thermal load, which is activated superlayer-by-superlayer. Each superlayer is sequentially activated, and an equivalent heat is applied to the newly activated superlayer to conduct the thermal simulation. In these methods, the thermal history on the path-scale level is assumed to be uniform so that it can be “lumped” or “agglomerated” on the layers.

For mechanical simulation, researchers developed the inherent strain method, which completely bypasses the laser scanning path. This method is a two-step approach. First, a full-scale simulation is conducted on a small sample domain to extract the effective "inherent strain." Then, multiple powder layers are agglomerated into a single "superlayer," where the simulation is conducted as a superlayer-wise activation process. The inherent strain method was originally proposed for welding problems based on the assumption that residual stresses would completely relax after the welding process [50]. However, this assumption is not valid for additive manufacturing, particularly in laser powder bed fusion, where non-uniform residual stresses are trapped due to complex scanning paths. Researchers have attempted to improve the inherent strain method to better account for the LPBF process. For example, a modified inherent strain method [48] was proposed to extract the inherent strain vector from a fine-scale model. This work has been further improved to use representative volume elements to address periodically layer-wise rotating scanning paths [49].

However, accurately predicting thermal history under more general scanning paths, complex geometry, and process parameters such as laser power and speed remains a challenge. The correlation between the thermal history and the scanning path, especially the sequence of melting and solidification, is often ignored. The loss of path-level information in thermal history, in turn, leads to inaccurate downstream simulations of, warping, residual stress, material properties, and the overall performance of the part [51, 52], to list a few. This is particularly problematic for the boundary regions of a layer and layers with intricate details, where the influence of the scanning path is more pronounced. For example, The effect of scanning strategies in the LPBF process is investigated in papers [38, 39, 40].

2.4 Discussion

In summary, the state-of-the-art LPBF simulation methods are either too computationally expensive for practical use or rely on assumptions that ignore the effect of the scanning path. Microscale simulations, which consider multiphysics and multiphase modeling such as the interaction between powders and melted metals, are too computationally intensive and applicable only to short paths. Voxel-based approaches simplify the problem into a solid thermomechanical issue, which is cheaper compared to microscale simulations, yet still impractical for engineering purposes due to the need for fine spatial and temporal discretization to capture the thermal and mechanical response of the moving laser. Layer-based approaches, which activate layers without considering the laser scanning path, are much more efficient but fail to account for the critical influence of the scanning path on material properties.

In contrast, I propose a framework to simulate the LPBF process that is efficient yet capable of accurately capturing the effects of the scanning path. This framework includes both path-level and layer-level simulations, which are synergistically integrated. The details will be introduced in the following chapters.

3 PATH-LEVEL THERMAL SIMULATION

3.1 Introduction

Many complex multi-physics and multi-phase phenomena are involved in the different stages of the LPBF process, including the initial melting of metal powders, the fluid dynamics and heat transfer of the molten metal, and the stresses and microscopic grain structure resulting from the solidification of liquid metals. These phenomena have important influences on the quality and performance of the manufactured part. As many of them are related to the thermal history of the part, an accurate and efficient thermal history simulation becomes critical to the understanding and improvement of LPBF processes. For example, thermal history influences the microstructure [15] and the material properties [16, 17]. The thermal history also influences the part's geometric accuracy through the residual stress, which is caused by uneven thermal expansion and shrinkage [29], which is closely related to the thermal history of LPBF parts.

The thermal history of a specific part is the result of its manufacturing process plan. The process plan includes processing parameters (e.g., the environmental and preheating temperature of the platform) and path-dependent scanning information including the power and speed of the laser. For a given geometric model, the build direction is determined first. Based on the process specifications such as the powder layer thickness, the geometric model is then sliced into layers normal to the building direction. Finally, the layers from slicing are filled with scanning paths, which direct the laser to scan the path segments with the given laser power. The scanning paths

have a critical influence on thermal history. For example, a given location might be melted once or remelted multiple times if different scanning paths are adopted. For a given geometric model, different combinations of possible building directions and scanning path results in an enormous degree of freedom on the path-scale level for process plan designing. The complexity of scanning patterns and the utilization of fast-moving and high-energy lasers in LPBF processes lead to complex heating/cooling and phase transitions, which complicates the thermal history across the entire part. Path-scale simulation approaches are critical to predicting the thermal history and exploring different process plans.

The contact-aware path-level (CAPL) discretization approach [53, 54, 55] was recently proposed to support scalable thermal simulation at the path level of AM processes driven by a moving heat source. Compared to other thermal simulation approaches, CAPL tailors discretization to the manufacturing toolpath and adopts locality for linear time complexity in part-scale thermal history simulations. This approach essentially uses scalable simulations to simulate the fabrication process of a part through the aggregation of melt pools, scan paths, and layers.

I developed a scalable PBF thermal simulation approach based on CAPL. CAPL tailors discretization to the manufacturing toolpath and adopts locality for linear time complexity in part-scale thermal history simulations. The new approach (will be referred as PBF-CAPL) inherits linear scalability from CAPL and has three novel ingredients. Firstly, to simulate the laser scanning on a solid surface, I discretized the entire simulation domain instead of only the manufacturing toolpath by appending the fictitious paths to the manufacturing toolpath. Secondly, to simulate the scanning

on the overlapping toolpath, the element widths were initialized by a Voronoi diagram of the manufacturing toolpath. Lastly, I proposed a modified conduction model that considers the high thermal gradient around the melt pool. I validated the new approach against melt pool images captured with the co-axial melt pool monitoring (MPM) system on the Manufacturing Metrology Testbed (AMMT) developed at the National Institute of Standards and Technology (NIST) [56, 57] [1]. Excellent agreements in the length and width of melt pools are found between simulations and experiments conducted on a custom-controlled laser powder bed fusion (LPBF) testbed on a nickel-alloy (IN625) solid surface.

The rest of this chapter is organized as follows. In Section 3.2, I identify and implement the needed improvements to account for the limitations of the original CAPL and specifics of the validation dataset.

In Section 3.3, I validate the simulation results against the experimental dataset that includes scan paths with varying laser power, where I find good agreement in the melt pool shapes between simulation results and the experimental dataset. In addition to comparing the melt pool images frame by frame, I also analyze various trends observed in the dataset. These include the influence of laser power on melt pool length, the melt pool length evolution on the same scanning vector, and scan-wise melt pool length evolution.

Based on the observation in Section 3.3, Section 3.4 discusses further improvements to CAPL-based thermal history simulation. These include the incorporation of the laser absorptivity model affected by surface roughness and keyholes and utilizing machine learning to determine melt pool shapes.

[1] The data used in this chapter can be obtained upon request from NIST.

3.2 Formulation

CAPL originally focused on the FDM process and made corresponding assumptions. Modification is needed to use CAPL to simulate the laser scanning on the solid surface. In this section, I first identify the modifications that are needed for CAPL to be consistent with implementation details in the NIST AMMT dataset. I then discuss the necessary modifications and improvements to address these discrepancies. (see Figure 3.1).

To attempt to improve the simulation results and better utilize and align with available data, I identified three needed modifications to be consistent with implementation details in the NIST AMMT dataset. Firstly, the original CAPL requires all the elements must be associated with a segment of scanning paths. The elements represent the powder materials that will be scanned and solidified. The widths of these elements will be dynamically grown in the execution stage to mimic the powder melting process. However, the AMMT data used is obtained on a solid surface. Because it is a continuum all the volume needs to be discretized and accounted for in the simulation no matter if scanning paths go through it or not. Also, since there is no powder melting process on the solid surface, the element growth is not applicable on the base layer.

Secondly, the original CAPL approach requires the element to have no overlap with other elements. The element contacts needs to be orthogonal since all elements have a similar rectangular shape. But in the PBF process, it is common to have overlapping paths since it is possible to remelt the solidified powder. In addition, the scan strategy used for the NIST experiment has nonparallel paths (see contour and infill in Figure

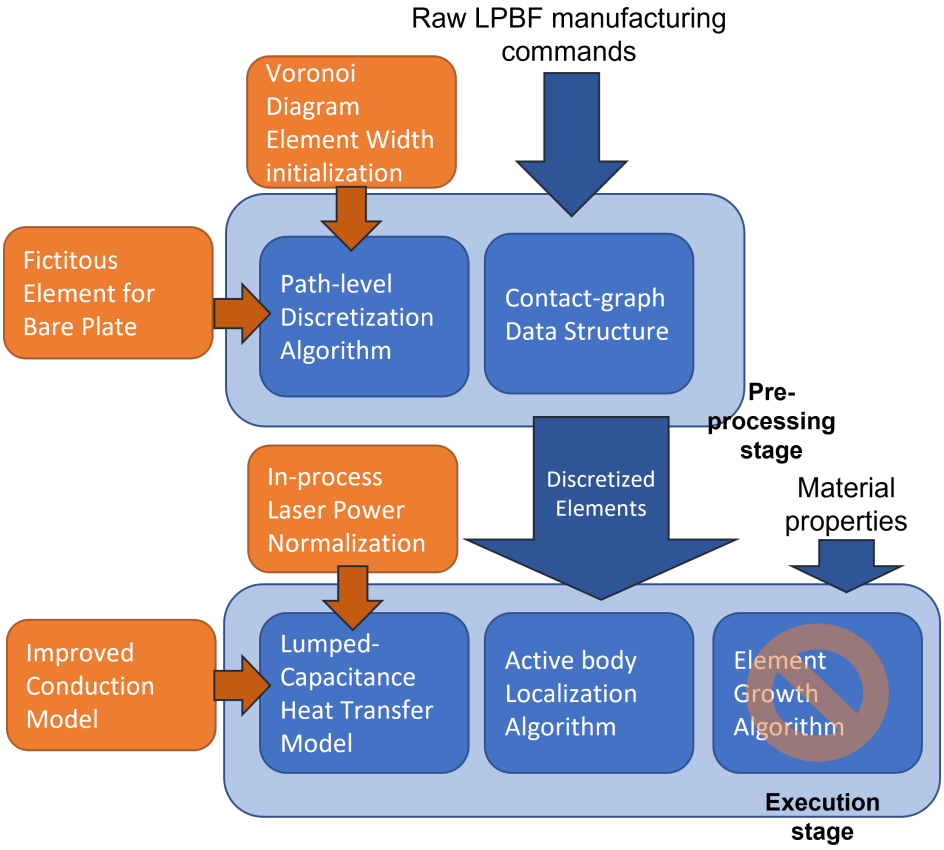

Figure 3.1: System diagram of contact-aware path-level (CAPL) for laser powder bed fusion (LPBF) process. The components of the original CAPL are in dark blue and my modification and improvements for validation are shown in orange.

3.2). Unexpected overlap or void will occur when addressing the general non-parallel paths, as shown in Figure 3.3.

Lastly, the original CAPL uses the forward Euler method (a first-order explicit method) for thermal simulation and assumes a small Biot number (Bi $= hL/k$, where h, L, k is the convection coefficient, characteristic length, and conductivity of the element) for the element. In the FDM process, elements usually can satisfy this assumption due to the scanning speed being relatively slow compared to the PBF

process. Here, however, a small element length ($\sim$10 μm) is required to ensure enough resolution to capture the melt pool length, but the element width is too large since the hatch space is too large (100 um here). This means the Biot number in the width direction will be an order larger than that in the length direction and should be reflected as such in a PBF model. In the lumped model, thermal conduction between two elements i and j is computed as $Q_{cond} = kA\Delta T_{ij}/d_{ij}$ where k is the conductivity, $A_{contact}$ is the conduction area, and $d_{ij}, and \Delta T_{ij}$ are the distance and temperature difference between the two elements. Considering the elements here (see Figure 3.3), a naive implementation of the lumped model will lead to insufficient heat conduction in the direction where the characteristic length is too long.

Representing solid surface with fictitious elements

For the first improvement, I modified the path-level discretization algorithm in the pre-processing stage to account for solid continuums. I added additional fictitious paths so that the entire domain is filled with real paths and fictitious paths. The contacts between all elements are initialized according to the contact graph. I initialized all elements with solid material properties since a solid surface is used in the present chapter. Since no powder melting is involved in the present chapter, I suppressed the element growth mechanism. For the present chapter, the fictitious paths are the contours around the real scanning paths, as shown in Figure 3.2.

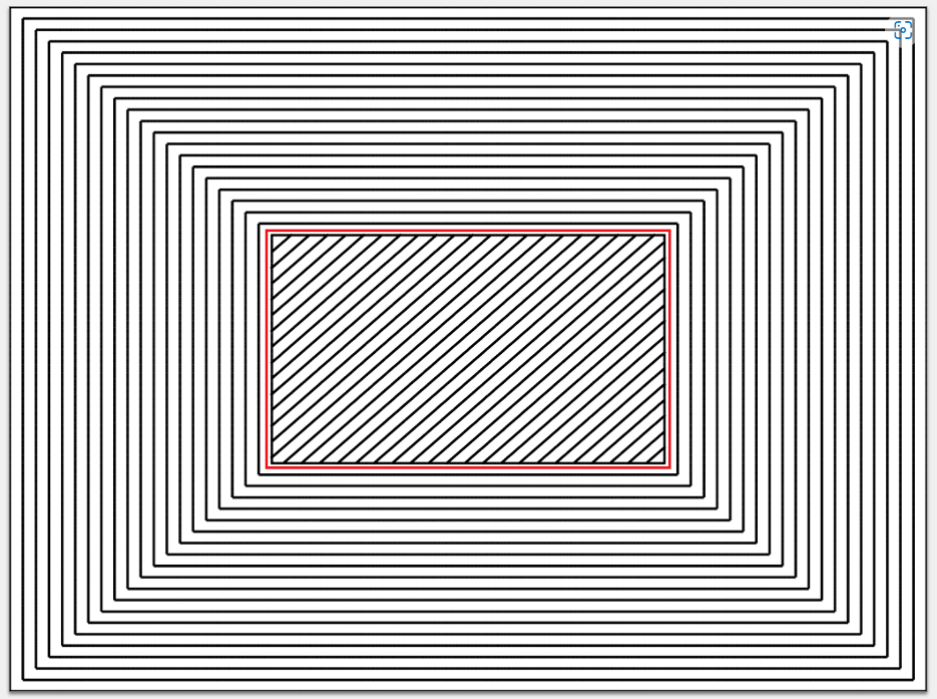

Figure 3.2: The actual laser path is inside the red box. Fictitious elements are added as the paths outside the red box to represent the larger surface. The solid continuum is modeled as multiple such layers.

Elements initialization by Voronoi diagram

To address the second improvement, I modified the path-level discretization algorithm with a new elements width initialization algorithm by the Voronoi diagram. The element width will be no longer updated in the execution stage since I suppressed the element growth mechanism as discussed above. In the new element width initialization algorithm, I initialized all element widths with a small number ($W_0 = 10\mu m$). After initialization, I increased the element widths simultaneously. For each element, I stopped the increase of width once the element's overlap with other elements exceeds a given threshold s ($3 \times 10^{-11} m^2$ used here). The element width initialization ends

when all elements stop growing wider. Such element width initialization procedure approximately generates a Voronoi diagram, whose cells have the path segments as their site, see Figure 3.3.

I used an in-process laser power normalization for the second needed modification in addition to the element width initialization by the Voronoi diagram. Note there are some overlaps and voids between the elements initialized by the Voronoi diagram. When a laser scans through these elements, the voids and overlaps will cause the total laser power input to artificially fluctuate. The in-process laser power normalization is a modification of the lumped-capacitance heat transfer model to correct for this artificial fluctuation. In the lumped model, every element takes the laser energy input. The total laser energy input on all elements should be equal to αP (laser power P multiplies absorptivity α) because of energy conservation:

$$\sum_{i}^{N} H_i(t) = \alpha P \tag{3.1}$$

where $H_i(t)$ is the laser energy input term of the element i. Theoretically N should be the number of all elements which are exposed to laser energy input. Here, I used the number of elements inside the active body as N. This approximation is due to the assumption of thermal localization by utilizing an active body. The total energy could be higher or lower than the input laser term because of the overlap and void. To mitigate this problem, I normalized the input laser power P during the simulation process by a constant $\alpha P / \sum_i^N H_i$. In other words, the laser power at t should be:

$$P(t) = \frac{\alpha P}{\sum_i^N H_i} P \tag{3.2}$$

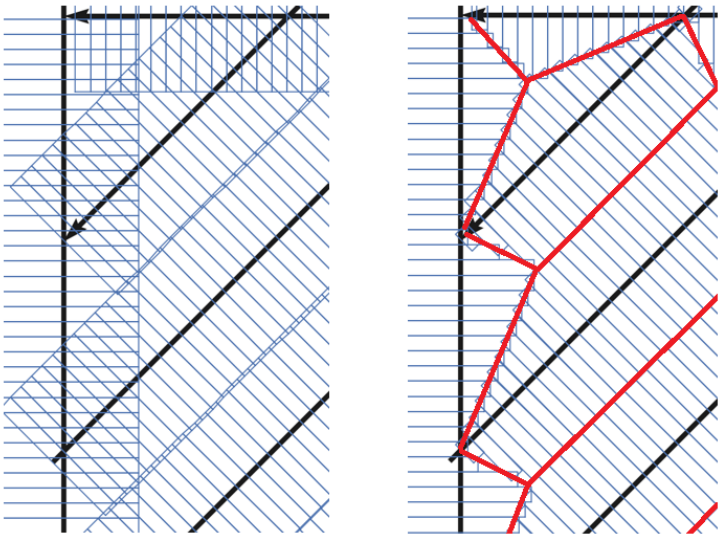

Figure 3.3: Example of elements on the left top corner of the layer. Unexpected element overlaps with non-parallel overlapped path exists before modification (left). Elements generated by Voronoi diagram after modification (right): elements (in blue) approximately form a Voronoi diagram (in red) whose sites are the scanning paths (in black)

in which P is the nominal laser power, and $P(t)$ is the normalized laser power to replace P in equation 3.1.

Improved conduction model

The third improvement addresses the lumped thermal model for the elements. Here I corrected a previously underestimated temperature gradient, which is originally approximated by the finite difference method. For example, the original conduction energy is given as $kA_{contact}\frac{\Delta T_{ij}}{d_{ij}}$, where the conduction characteristic distance is d_{ij}

which is the distance between two elements i and j. In a real melt pool, the temperature spatial gradient is very high around the melt pool (temperature spatially decays from the melting point to a much lower temperature in a relatively short distance). When the element width is too large, the same temperature decay will be artificially assumed to happen at a much larger distance (the element width), thus the side-by-side conduction will be underestimated. To address this issue, I capped the conduction characteristic distance by thresholding the conduction characteristic distance. Here I assumed the threshold d_0 to be a constant which equals to the maximal element length (here is 10 um). Since here element length is much smaller than the element width, the threshold d_0 ensures the thermal conduction Q_{cond} in both the scanning direction and the transverse direction has the same order of magnitude. The conduction term between two elements i and j is to be modified as

$$Q_{cond} = \frac{kA_{contact}\Delta T_{ij}}{\max(d_0, d_{ij})} \tag{3.3}$$

Due to the existence of overlapped elements, I redefined the contact area as the projection area (the projected angle is θ) of the intersected cross-section (see Figure 3.4):

$$A_{contact} = \min(A_{cs1}, A_{cs2})/\sin\theta \tag{3.4}$$

where $A_{cs} = W \times H$

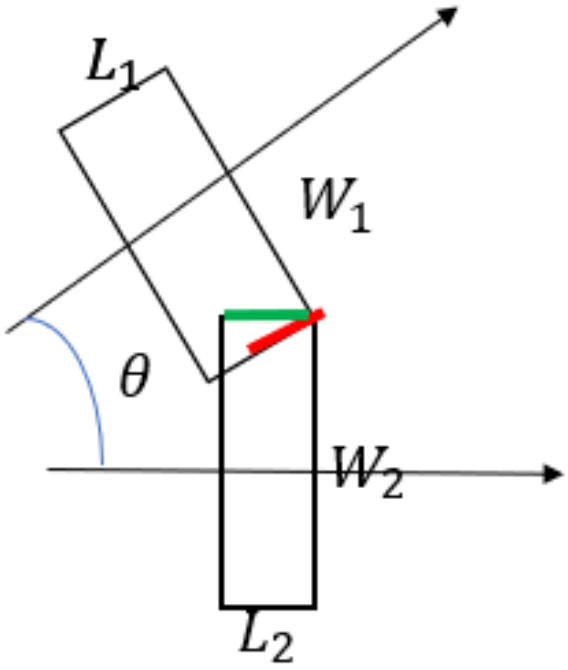

Figure 3.4: Top view of the contact area (in red). The contact area is the smaller projected cross-section (in green) projected along the angle θ between two elements. L and W are the element length and width. Arrows indicate the scanning directions.

Assumptions and limitation

I used some common assumptions that are typically employed in the common voxel-based approaches. For example:

- Deformation is small, allowing for the thermal and mechanical simulations to be decoupled, and in-process deformation is not considered.
- All materials, including powder, liquid, and solid, are represented as solids with modified properties, avoiding fluid and other multiphase problems.

- Mass loss due to evaporation is ignored.

Besides these common assumptions, the most important assumption is related to the use of the lumped model. By using the lumped model, I assume the temperature within an element is completely uniform in space. Similar assumptions are made in other voxel-based approaches, but the difference is that, due to the lumped model, the elements in the proposed approach are much larger. Therefore, I must modify the lumped model to consider these effects. For example, as previously discussed, an improved conduction model has been introduced since using finite differences to represent the thermal gradient is not accurate. Additionally, in some circumstances, the thermal response might differ, such as the difference between the conduction mode and the keyhole mode, which needs to be considered. In the last section of this chapter, I will discuss how I used a modified absorptivity model to account for this. Essentially, this is a problem of localization: we need to understand how the problem can be localized near the heat source and how the localized model corresponds to the lumped model.

3.3 Validation through melt pool shape

Validation Dataset Overview

The experiment dataset used for validation of the modified CAPL consists of melt pool frames acquired on the Additive Manufacturing Metrology Testbed built by NIST. The resolution of each frame is approximately 7.13 um/pixel. An example of the melt pool frame is shown in Figure 3.5. A threshold of the digital value corresponding to

Figure 3.5: An example of melt pool frame (left) acquired on the Additive Manufacturing Metrology Testbed by NIST and the binarized result (threshold is 80 out of 255).

the melting temperature is needed to extract the melt pool shape. Based on other experiments conducted on AMMT [57], I used 80 out of 255 as the threshold (see Figure 3.5). The melt pool shape is approximated by the Python library scikit-image's skimage.measure.regionprops function (equivalent to MATLAB's regionprops function), which approximates the melt pool shape by an ellipse that has the same normalized second central moments as the region. The melt pool length and width are computed as the length of the major and minor axis.

I used the first 10 cases from the dataset with varying laser power and every case consists of 1498 melt pool images at various locations during the laser scan. The scanning paths are shown in Figure 3.6 and all 10 cases use the same scanning path. There are in total 39 scan vectors which are labeled in Figure 3.6. The laser scanning speed for all 10 cases is the same and is shown in Figure 3.7. Note the laser is turned off while overshooting outside the scanning region to ensure constant scanning speed inside the scanning region. For ease of discussion, I classified scan vectors into different groups, including 4 contour vectors and 35 diagonal raster scan vectors inside the contours (see Figure 3.6). The 10 cases differentiate from each other

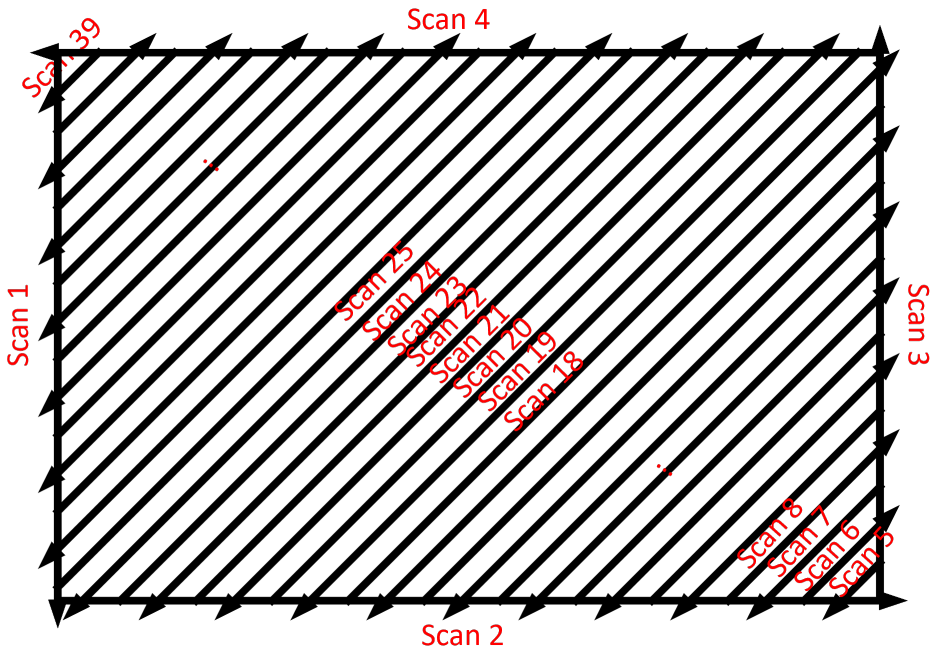

Figure 3.6: Numbering of scan vectors.

by the laser power being used (see Figure 3.8). Case 01 has the highest laser power which is constant (195 W), and all other cases have variable and lower laser power. For example, the laser power of Scan 01 for all cases and the laser power of Scan 19 - Scan 24 for Case 03 are shown in Figure 3.9, in which the laser power is plotted as a function of the distance along the scanning direction. The laser power was lowered to decrease the variance in melt pool size based on the residual heat factor in an earlier NIST study. Interested readers may refer [57] for details. For every case, the 1498 melt pool images come from sampling on a single-layer scanning on an Inconel 625 solid surface. The images come from an even sampling at the frequency 20kHz when the laser is turned on.

All melt pool lengths from the experimental melt pool image data are plotted as

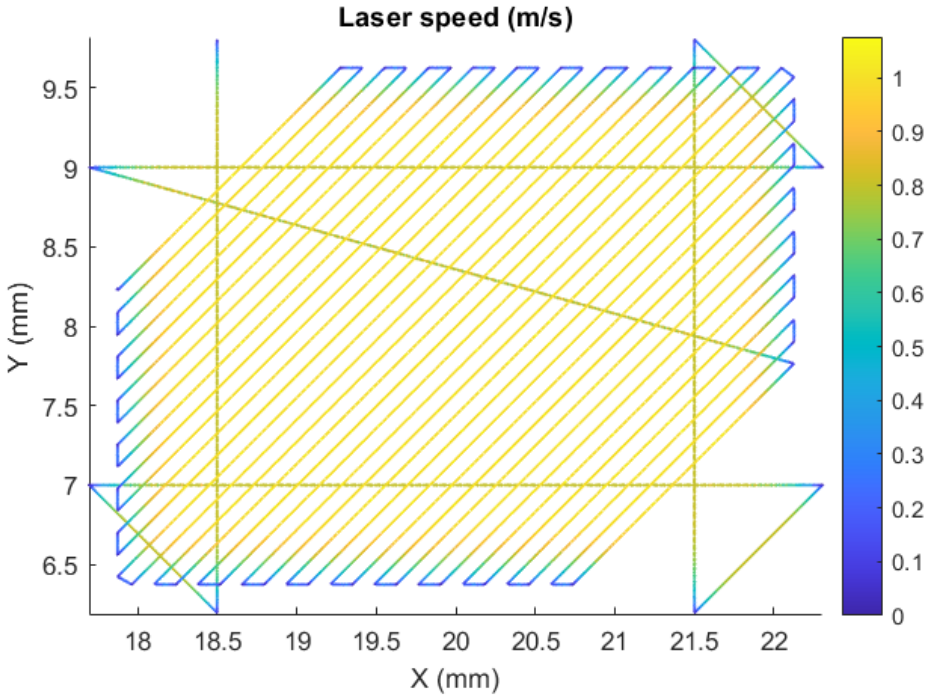

Figure 3.7: Laser speed map for Case 01. All 10 cases have the same identical speed map only different by their relative locations. Only Case 01 has constant laser power.

line graphs shown in Figure 3.10. The vertical axis represents the melt pool length, and the horizontal axis represents the frame number. Since the scanning path is geometrically the same for all cases and the frames are sampled at the same time sequence, the same frame number results in the same relative location in every case.

In all cases, I observed that the melt pool lengths periodically drop to zero. This is due to a synchronization issue of the melt pool monitoring system such that the first image at the beginning of each scan is captured before the laser starts. In addition, excessively long melt pools are observed near the beginning of some scan vectors.

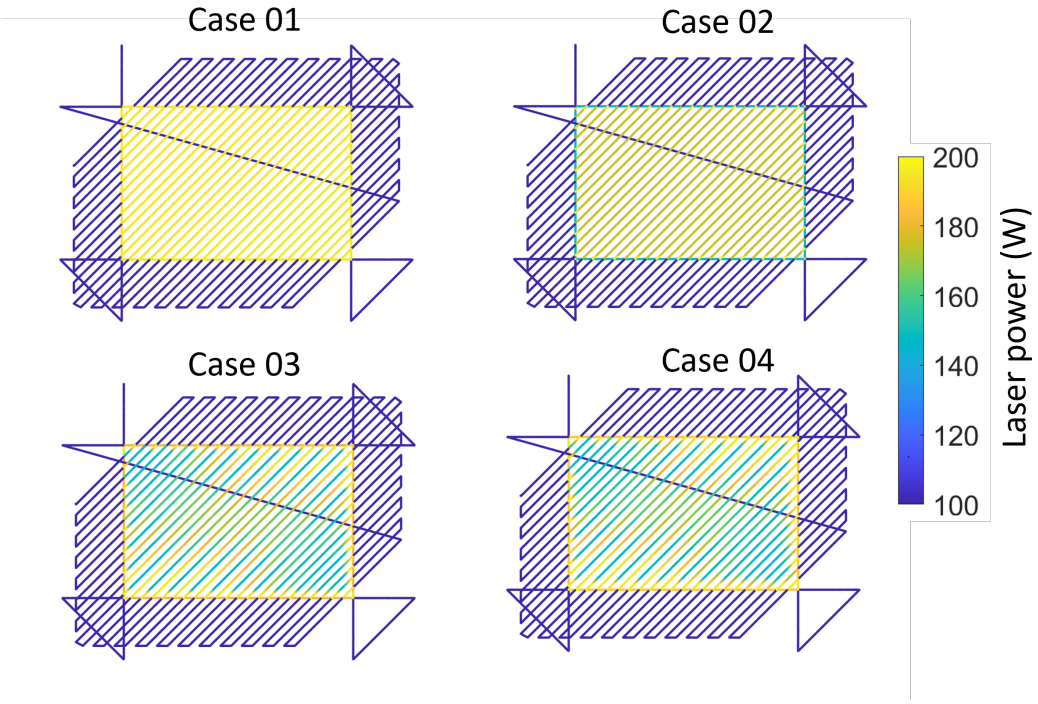

Figure 3.8: Laser power map for cases 01 - 04. The dark blue here indicates no power. From Case 02, all cases have variant laser power and they differentiate from each other by how the laser power distributes.

Upon closer examination, this is due to the gas plume being mischaracterized as the melt pool after thresholding (see Figure 3.11). In both these cases, the extracted melt pool lengths do not correspond to the real melt pool length, therefore, are considered outliers in the CAPL validation.

Calibration of process parameters and material properties

Melt pool length from CAPL simulation is directly computed by measuring the maximum distance between two melted elements. I used all material properties but absorptivity from [1] for simulations in the present chapter. Material properties

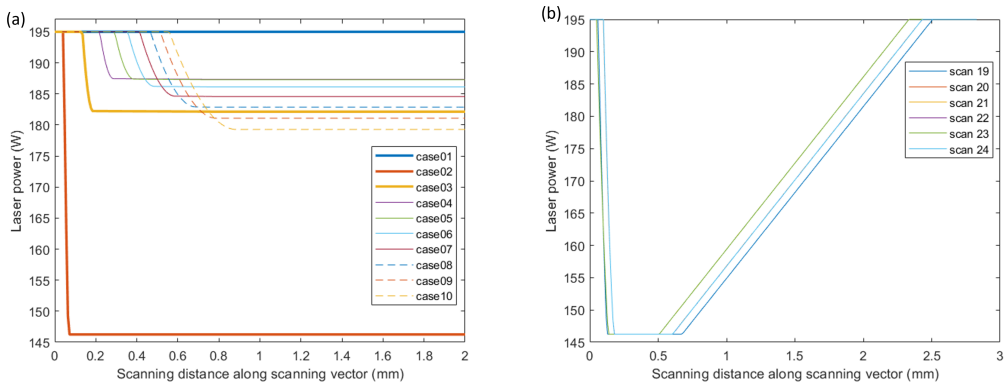

Figure 3.9: Laser power plotted as a function of distance along the Scan 01 for all cases (a). The distance range from 0 to 2 mm because the length of Scan 01 is 2 mm for all cases. (b) The laser power of Scan 19 - 24 for Case 03. Scan 19 - 24 have adjacent parallel scan vectors which have the same length.

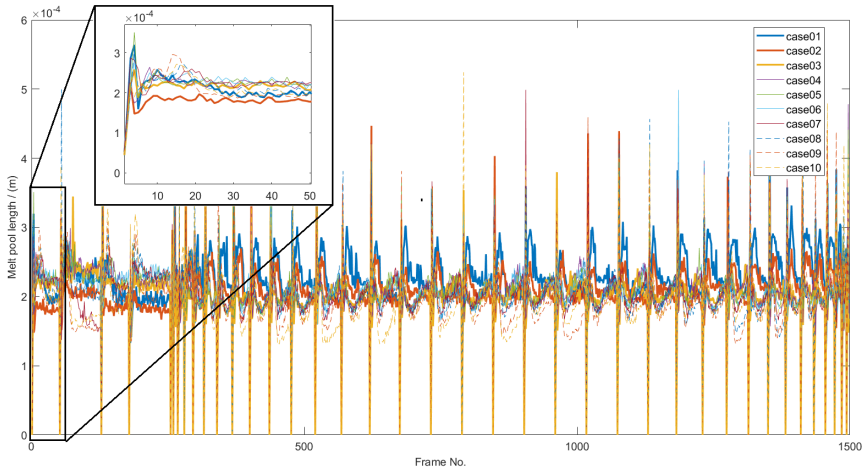

Figure 3.10: Experimental melt pool length for all 10 cases $\times$ 1498 frames. Zoom in view of Scan 01 is shown. Zero melt pool length is due to the MPM system skipping the first frames of the scan vectors.

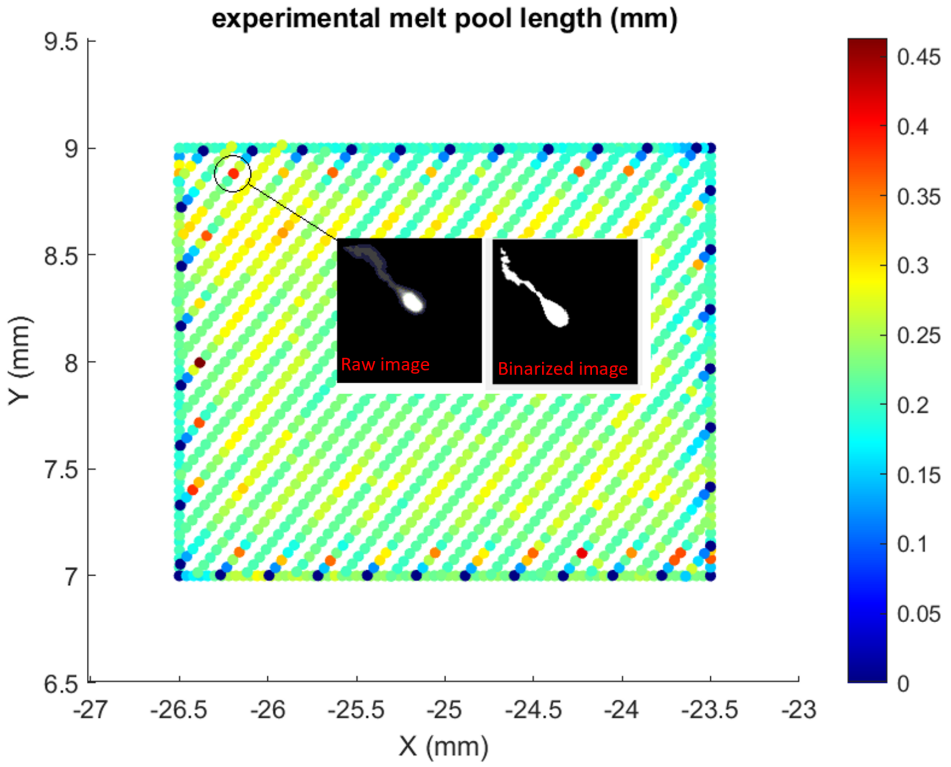

Figure 3.11: Melt pool image with plume and the binarized results (threshold is 80). Plume leads to incorrect melt pool length extracted value. These incorrect values are shown in the length map as red dots.

including specific heat and conductivity are modeled as functions of temperature (see table 3.1). Phase changes due to melting or solidification are handled by the equivalent specific heat formulation [1, 58].

The absorptivity is calibrated with Case 01 of the dataset and used for the remaining cases. I calibrated absorptivity because it has a significant influence on thermal history and it can significantly vary when the surface conditions vary. Understanding absorptivity and surface conditions itself can be an important topic where many studies have been conducted [59, 60]. I noted that the absorptivity of laser power

may depend on a variety of factors and is not a constant in general, but it is a common practice that constant absorptivity is used for simplification. In the present chapter, I chose 0.43 as it minimizes the error of melt pool length in Case 01. This value is consistent with the ranges provided by the literature. For example, the absorptivity of In625 solid surface ranges from 0.4 to 0.9 [61]. This value is applied to other cases in the subsequent tests.

Experimental data and simulation results of melt pool lengths, as well as the error percentages, are plotted in Figure 3.13. I observed a consistent match between the experimental data and simulation results with about 10 percent of average relative error in all cases as shown in table 3.2. In the table, the error value is the mean of the absolute value of the relative error of all data points in each case. In addition, Figure 3.12 shows the distribution of the relative errors for Case 05 where 84% of data points are within 10% relative error and 92% of data points are within 20% relative error compared to the experimentally acquired meltpool image data. The histogram also shows that the distribution of the relative error skews towards the underestimation of the meltpool length. This could be due to the inclusion of plumes that increase the length of some meltpools as an artifact (see Figure 3.11). Further comparisons between simulation results and experimental data will be discussed in detail in the rest of this section.

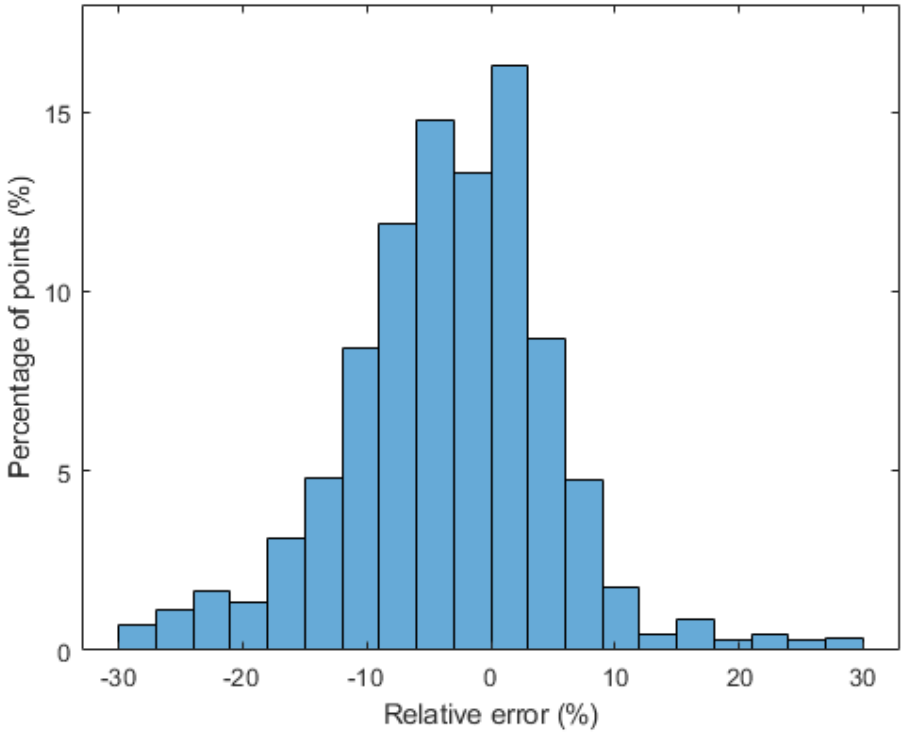

Figure 3.12: The histogram of relative error in percentage of Case 05. The y-axis is the percentage of the data points in case 05. 84% of data points are within 10% relative error and 92% of data points are within 20% relative error.

Table 3.1: Process parameters and material properties of IN625[1]

Solidus temperature T_S	1563 K
Liquidus temperature T_L	1623 K
Environmental temperature	293 K
Latent heat of fusion	290 kJ/kg
Specific heat ($T \leq T_S$)	338.98 + 0.2437$\times$ T [J/kg K]
Specific heat ($T \geq T_L$)	735 J/kg K
Thermal conductivity, ($T \leq T_S$)	5.331 + 0.015 $\times$ T [W/(m K)]
Thermal conductivity, ($T \geq T_S$)	30.05 W/(m K)
Density	8440 kg/m^3
Environmental convection coefficient	10 W/(m^2 K)
Substrate temperature	293 K
Laser spot diameter	85 um

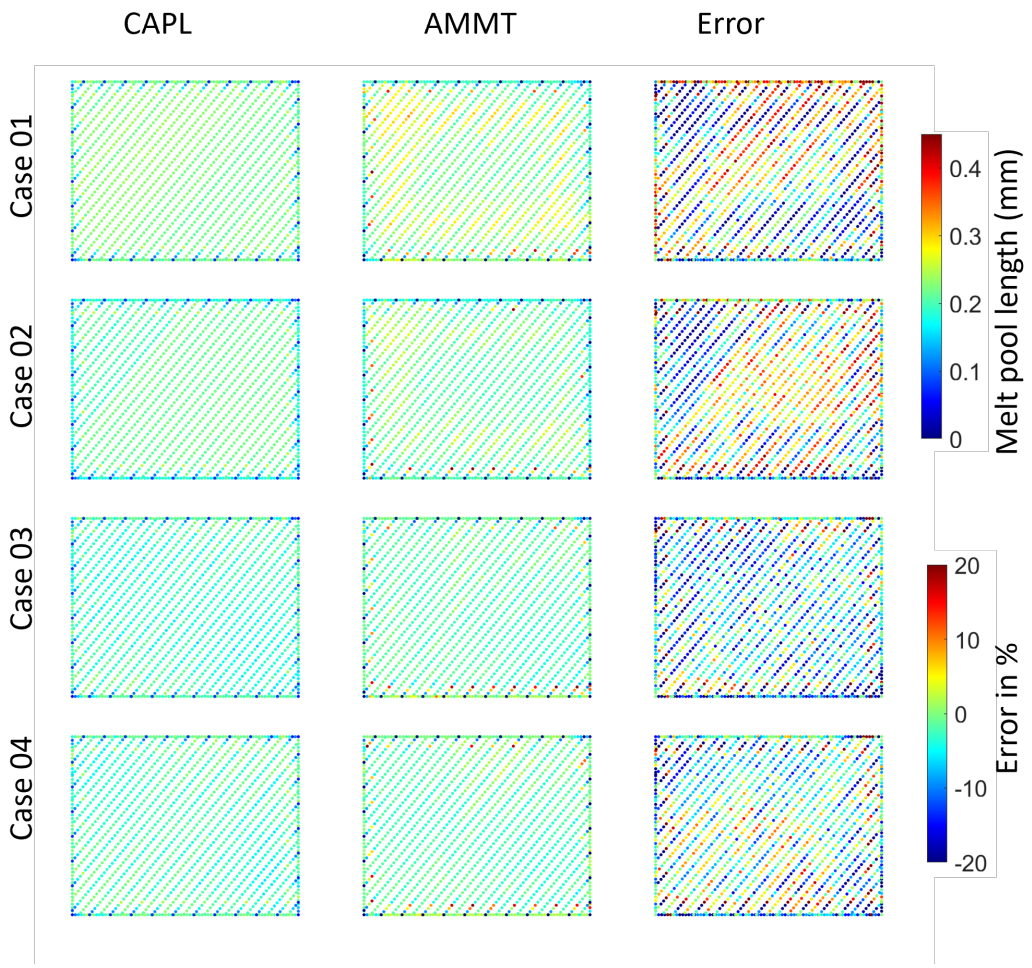

Figure 3.13: AMMT experimental results of melt pool length map for cases 01, 02, 03, and 04 (middle) and the corresponding CAPL simulation results (left) and the relative errors in percentage (right). AMMT and CAPL results share the same color bar.

Melt pool length validation

Melt pool length evolution within scan vector

Firstly I will discuss the melt pool length evolution on the same scan vector. I will categorize the results into two groups: contour scan vector (I will use Scan 01 as an example) and 45-degree scan vector (I will use Scan 19 - 24 as examples).

I chose Scan 01 since it can be considered a single-scan test without thermal inference from other scan vectors. Because it is the first scan vector and there is no laser scanning on the surface yet before Scan 01 is applied, Scan 01 should be free from the influence of other scan vectors. Therefore the evolving melt pool shape on it should just reflect the influence from Scan 01. I also chose Scan 19 - 24 in Case 01 because (a) they are parallel and identical to each other and all scan vectors have constant laser power, and (b) I observed melt pool length evolves similarly on these scan vectors (see Figure 3.15).

On Scan 01, I plotted melt pool length as a function of scanning distance on the scan vector and show the results of cases 01 in Figure 3.14. An increase in melt pool length at the beginning of the laser scan, i.e. "bump", is observed in Case 01: melt pool length firstly increases and then decreases as the laser moves on the scan vector. I also observed the bump on the 45-degree scan vectors (see Figure 3.15) of Case 01. The CAPL simulation does not predict such a bump in these cases. One possible reason for this discrepancy is that I used constant absorptivity in modified CAPL simulation. This is because I observed that the magnitude of the bump is related to the laser power. For example, comparing the melt pool length on Scan 01 in different cases, the bump is much less obvious in cases 02 - 07, where relatively lower power

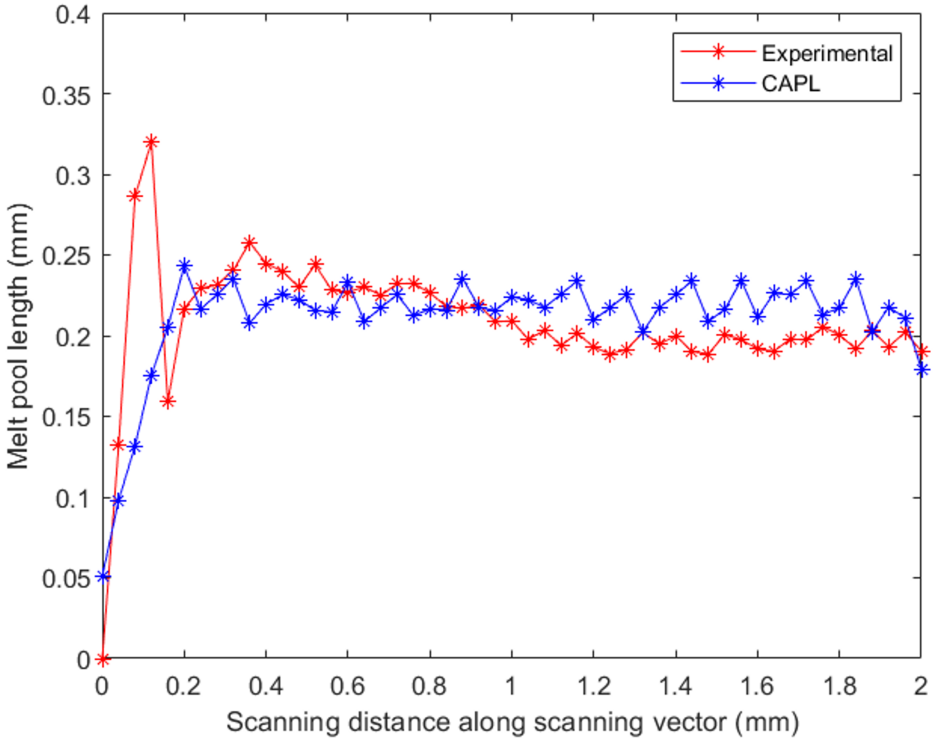

Figure 3.14: Melt pool length for Scan 01 of Case 01. A bump at the beginning of the scan vector in experimental data is not predicted by CAPL in Case 01. Laser power along the scan vector can be found in Figure 3.9.

is applied shortly after at the beginnings of the scan vectors. The CAPL simulation matches well with experimental data in these cases (see Figure 3.16 and Figure 3.17). I will discuss the increase in melt pool length at the beginning of the laser scan in Section 3.4.

The effects of varying laser power on the length of the melt pool are also predicted by the CAPL simulation. I give examples in Figure 3.18, where the mean values of melt pool length on Scan 01 and Scan 24 are plotted with respect to the case number. I observed that CAPL captures a similar trend as shown in experimental data: on

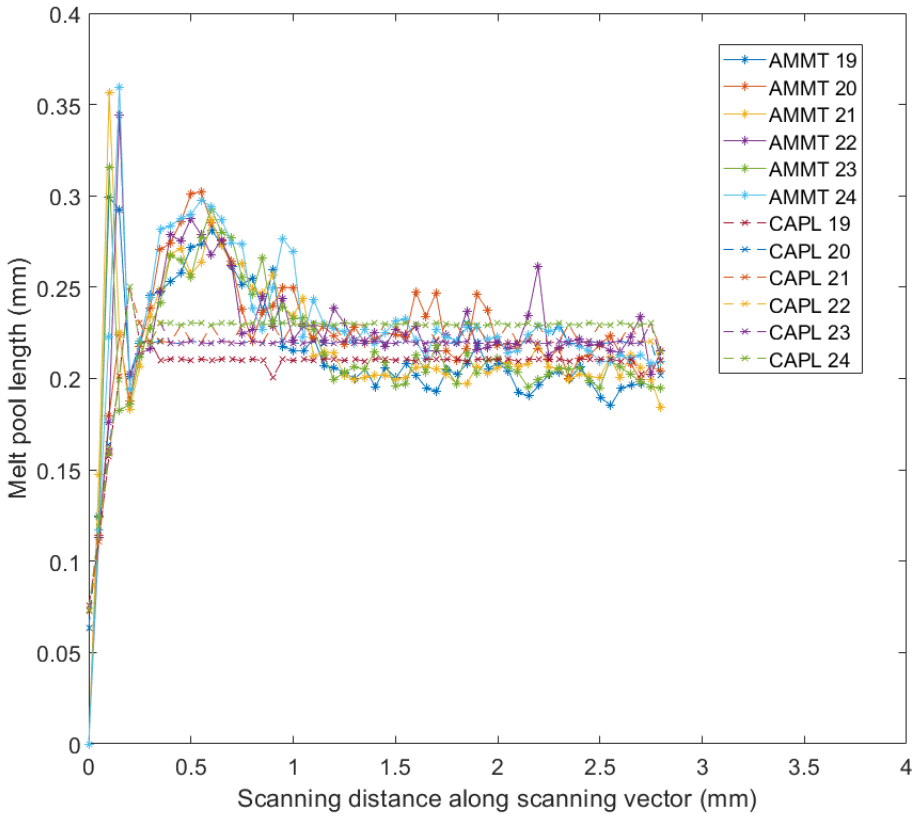

Figure 3.15: Experimental (AMMT) and simulation (CAPL) melt pool length of Scan 19-24 for Case 01. Laser power is constant (195 W). The CAPL approach does not predict the bump.

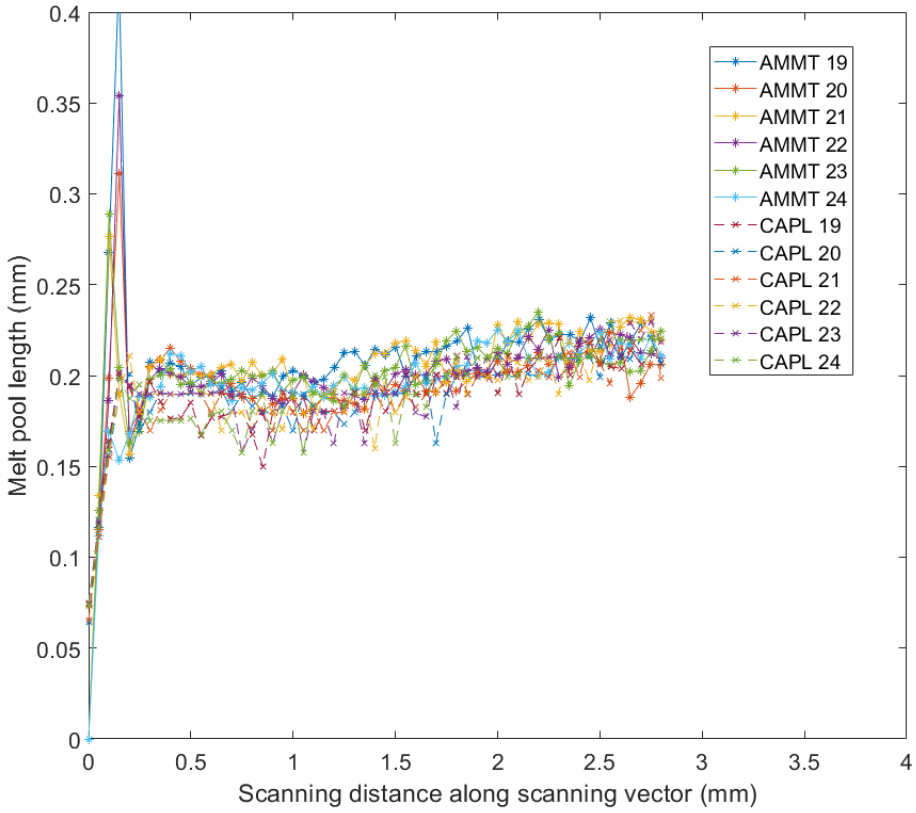

Figure 3.16: Experimental (AMMT) and simulation results (CAPL) of Scan 19 - 24 in Case 03. The bump disappeared in experimental data, and the trend in experimental data is captured by simulation results. The laser power of these scans can be referred to in Figure 3.9.

Scan 01, Case 02 has the smallest average melt pool length, and then the average melt pool length increases from Case 03 and then decreases again from Case 07. On Scan 24, both CAPL and experimental data suggest the smallest average melt pool length is in Case 09 and the largest average value is in Case 01.

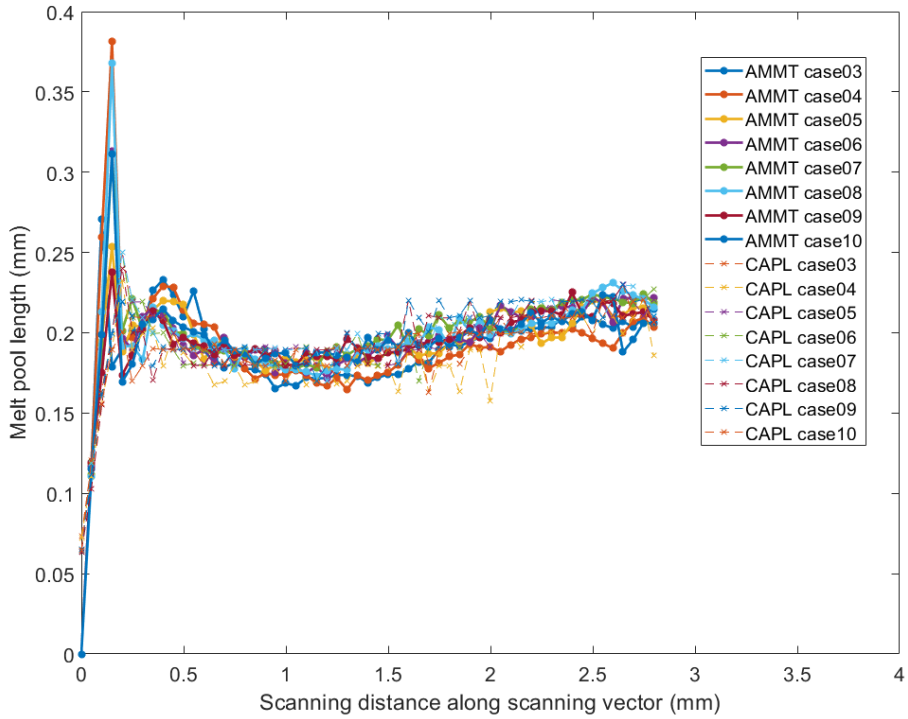

Figure 3.17: Scan 19 in Case 03 - Case 10 as a function with respect to scan distance. AMMT data vs CAPL simulation results.

Scan-wise melt pool length evolution

In this section, I will discuss the melt pool length evolution across the scan vectors. The average melt pool length of each scan vector is shown in Figure 3.19. From Scan 05 to Scan 39, melt pool lengths first increase, then plateau, and finally drop. This trend is consistent with the lengths of these scan vectors. The length of the scan vector starts as short with Scan 05 at the right bottom, reaches the maximum at Scan 19 and plateau, and decreases again to the last Scan 39. The scan vector averaged melt pool length is short when the total scan vector length is short and vice versa. This is

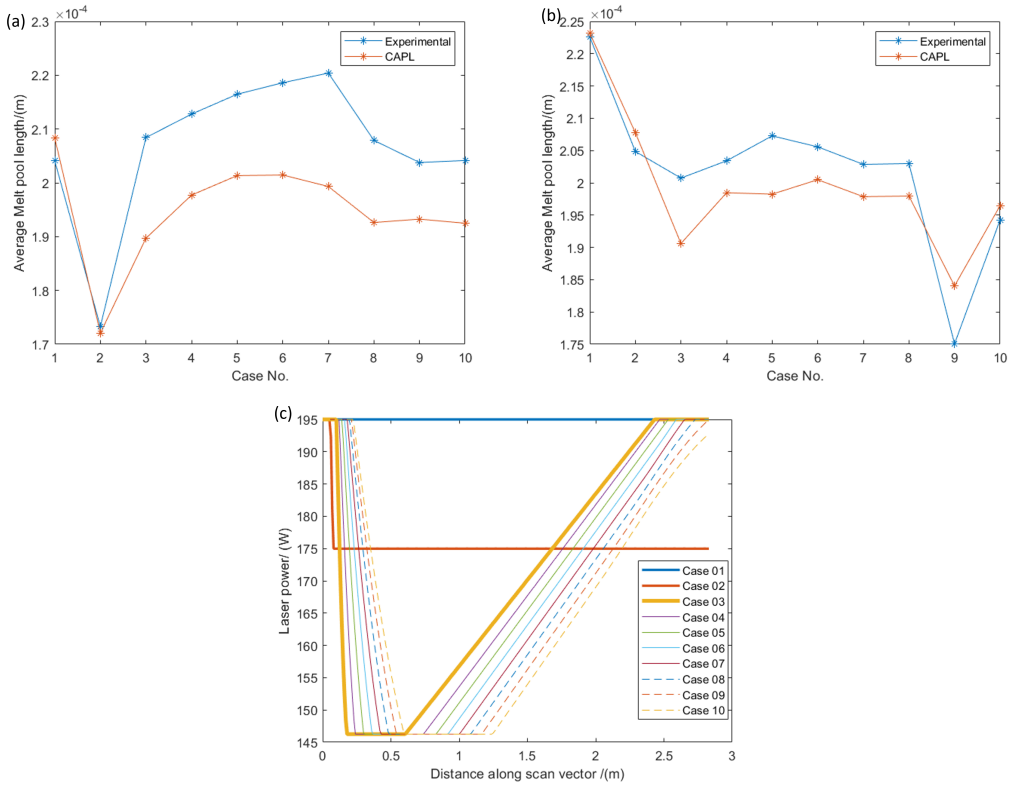

Figure 3.18: Mean value of melt pool length on Scan 01 (a) and Scan 24 of Case 01 to Case 10 (b) and laser power on Scan 24 (c). CAPL predicts a similar result compared with experimental data.

because the melt pool needs the scan vector to be long enough to have its tail formed. On each scan vector, the melt pool always starts with a relatively round shape and gradually evolves into a tear shape as the laser moves (see Figure 3.20). A scan vector that is too short will be dominated by the melt pool shape without tails.

The scan vector length is not the only factor that affects the melt pool length. In both the experiment data and modified CAPL simulation results, I observed some trends which could be explained by the influence of reheating from adjacent scan vectors. As shown in Scan 19-24 in Case 01, the difference in melt pool length between

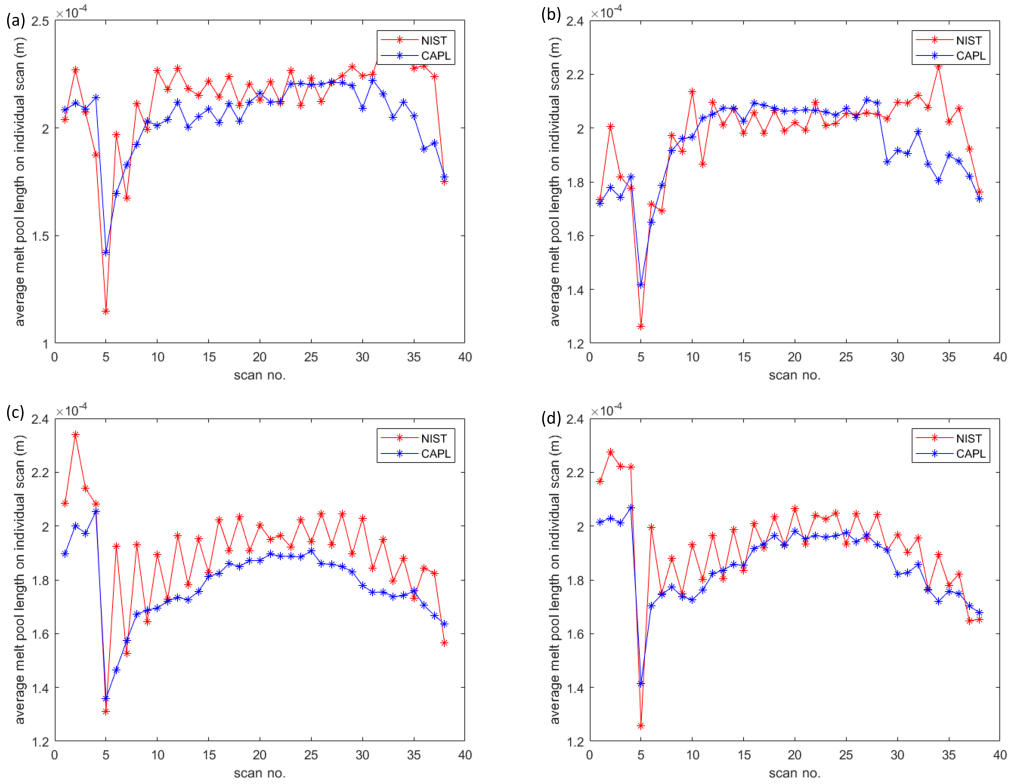

Figure 3.19: Scan-wise average melt pool length, Case 01, 02, 03, 05 in (a), (b), (c), and (d). The oscillation of experimental data is due to the perturbation of plume frames.

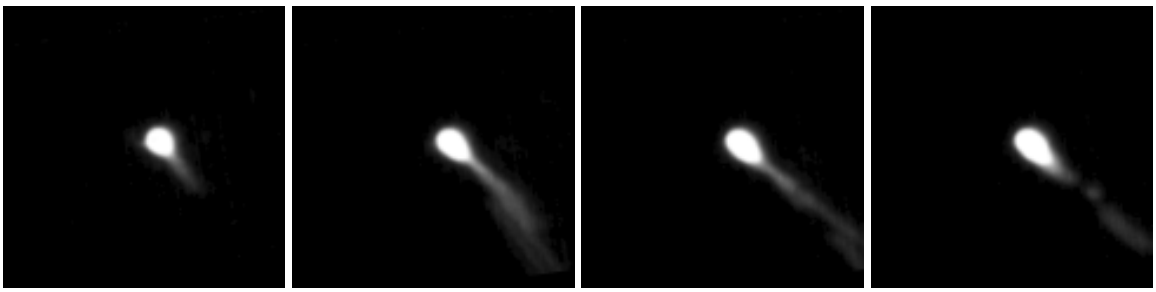

Figure 3.20: Experimental frames of Scan 39 in Case 01. Scan 39 is the last scan vector and only has four melt pool frames. The melt pool evolves from a relatively round shape to a tear shape.

Table 3.2: Relative error of melt pool length predicted by CAPL

Case No.	01	02	03	04	05
Relative error (%)	11.11	9.80	9.62	8.81	8.44
Case No.	06	07	08	09	10
Relative error (%)	8.21	8.87	9.03	11.66	12.70

the neighbor scan vectors seems negligible. It seems the reheating from the adjacent scan vectors is negligible since Scan 24 has a comparable melt pool length to that in Scan 19. However, it is interesting to note that, even though they have identical scan vector lengths, Scan 39 always has a longer melt pool length compared to Scan 05. Note that Scan 05 is the first 45-degree scan vector and Scan 39 is likely due to the accumulation of residual heat in the scanning progress. Similar situations can be also found in other cases, see Figure 3.19. This also might be due to the reheating from the adjacent scan vectors, and this effect is only significant at the beginning of the scan vector where the melt pool is relatively round without a tail.

Melt pool width validation

The CAPL simulation results cannot be directly used to obtain the melt pool width because they are only defined on the scanning paths. In the present chapter, I obtained the melt pool width from the reconstructed melt pool based on the CAPL simulation results. I reconstructed the melt pools by using inverse distance weighted interpolation of temperature distribution. Since the temperature for every element at any specific time is available, the temperature at any location can be given by

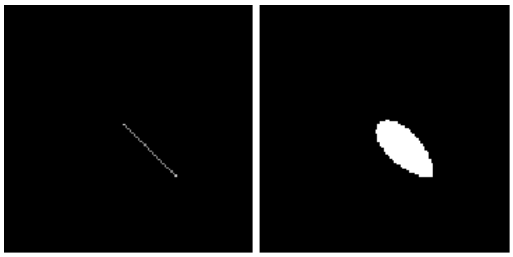

Figure 3.21: Melt pool from CAPL (left) and its interpolation (right).

interpolation:

$$T(x) = \frac{\sum_i^N w_i(x) T_i}{\sum_i^N w_i(x)} \tag{3.5}$$

where $w_i(x) = \frac{1}{d(x,x_i)^p}$ is the power p of the inverse of distance between element i and location x (I used $p = 1.3$ here which minimizes the errors). N is the number of elements inside the active body. In the present chapter, I interpolated the melt pool shape on a 0.96 mm $\times$ 0.96 mm region with a 120-pixel $\times$ 120-pixel frame. An example of such interpolation is given in Figure 3.21. I obtained the melt pool width by the same approach used for experimental melt pool width with the interpolated temperature distribution: melt pool width is the length of the minor axis computed by the regionprops function with the given interpolated temperature distribution.

Melt pool width from the experiment dataset and prediction by CAPL through interpolation and the relative errors are shown in figure 3.22. The averaged relative errors for all cases are reported in table 3.3. The melt pool width has less variation compared with the melt pool length. For example, the melt pool width evolution of the Scan 19 is plotted as a function of scanning distance along the scan vector in

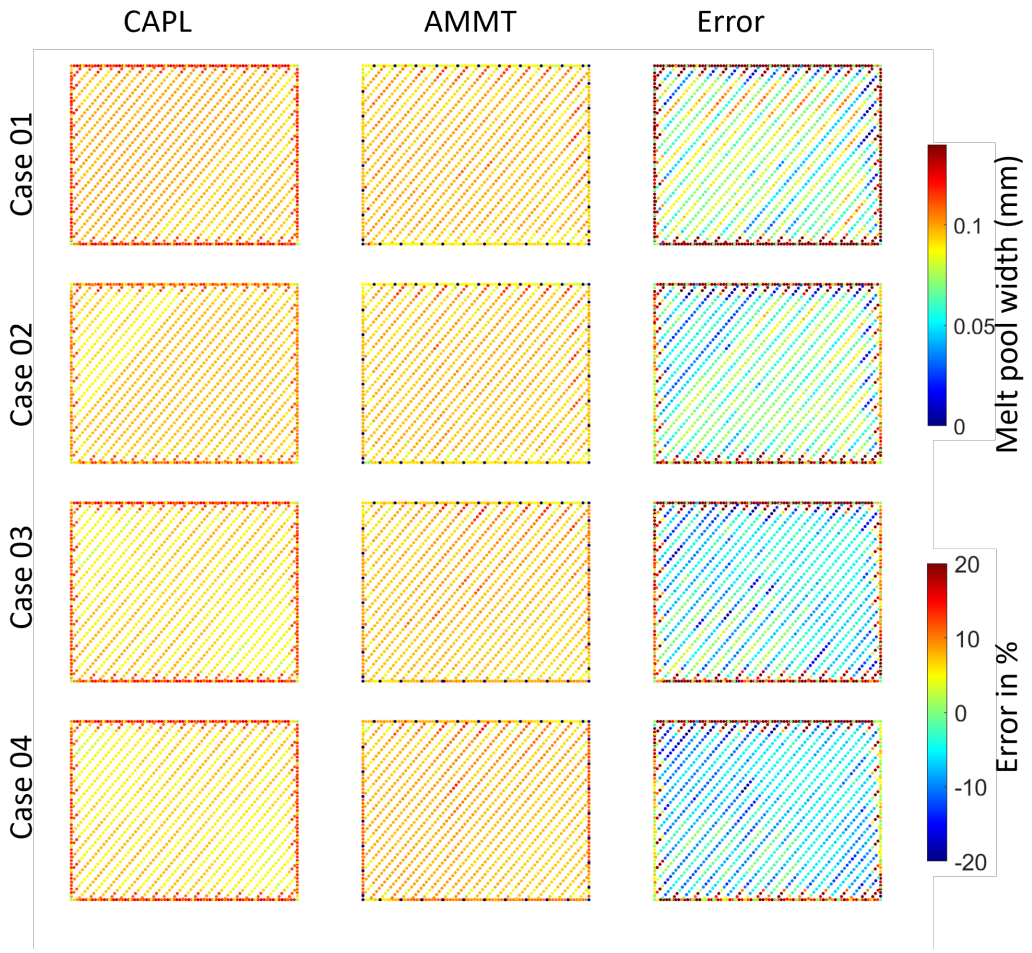

Figure 3.22: Experimental (AMMT) melt pool width map (middle), the interpolation results based on CAPL simulation results (left), and the relative errors in percentage (right) for cases 01 - 04. AMMT and CAPL results share the same color bar.

Figure 3.23). Note that laser power is not constant in Cases 02, 03, and 05, but both CAPL simulation results and experimental data suggest melt pool width has very little variation compared with the melt pool length in a scan vector like it is in Case 01 (see Figure 3.15), indicating that the melt pool width is less sensitive to laser power than the melt pool length.

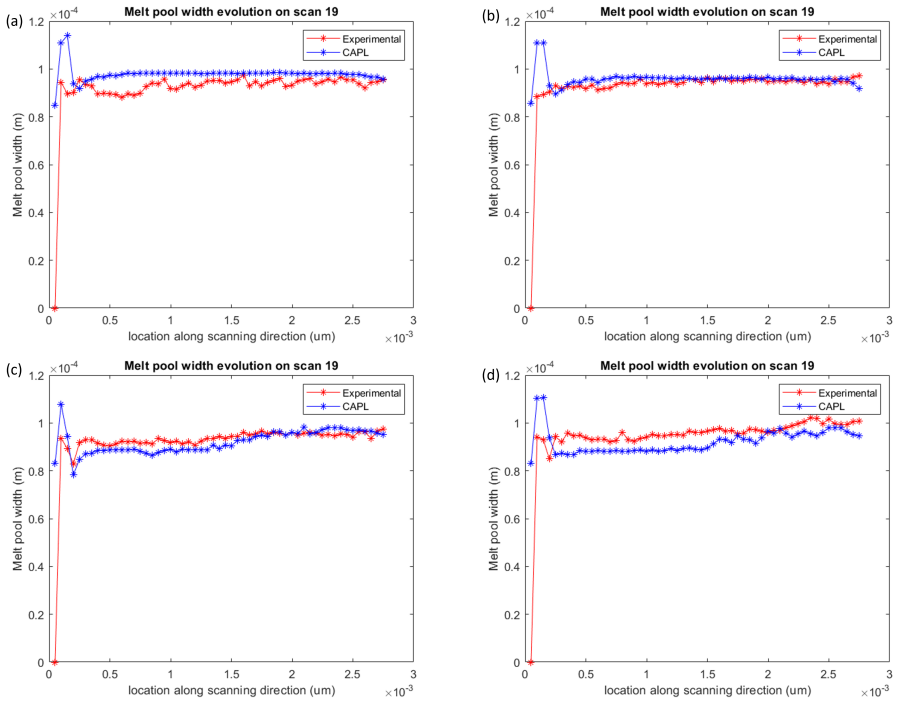

Figure 3.23: Melt pool width on Scan 19 of Cases 01, 02, 03, and 05 in (a), (b), (c), and (d). Both experimental data and CAPL simulation results show a relatively constant evolution.

Table 3.3: Relative error of melt pool width predicted by interpolation of CAPL results

Case No.	01	02	03	04	05
Relative error (%)	9.80	6.93	8.62	8.753	9.50
Case No.	06	07	08	09	10
Relative error (%)	9.90	10.64	9.99	13.71	9.36

3.4 Discussion

In this chapter, I developed an path-scale PBF thermal simulation approach based on contact-aware path-level (CAPL) discretization. I validated the proposed approach with melt pool shapes acquired by the Additive Manufacturing Metrology Testbed (AMMT) built by the National Institute of Standards and Technology (NIST). I demonstrated that the proposed approach achieves a good match of the melt pool length and width compared with the experimental data. I also discussed the influence of laser power on the thermal history at the path-scale level.

One source of error during the CAPL validation is the increase in the difference in melt pool length at the beginning of the laser scan while the laser power and speed remain constant in Case 01. This is likely due to the use of constant absorptivity in the current work, which is widely assumed among LPBF thermal history simulations [45, 62, 63]. Such an assumption results in an underestimation of the absorptivity at the beginning of high-power scan vectors during the calibration, for example in Case 01 and Case 09 (see Figure 3.25). Experimental measurements have observed absorptivity to change throughout the laser scan path [59, 61, 3]. For example, a distinctive four-stage change in laser absorptivity has been identified for heating a stainless steel plate [3]: (a) an initial rise due to the shiny plate melting increasing surface roughness, (b) a subsequent drop due to the liquid melt pool formation and increased reflectivity, (c) the second rise due to the formation of the keyhole, and (d) eventually a keyhole-related high-frequency periodic oscillation. A dynamic laser absorptivity depending on the time and distance of the laser start as well as the condition inside the meltpool therefore will better capture the melt pool behavior

near the beginning of the laser scan.

Based on this observation, I created a simplified model that captures the laser absorptivity trend in stages (a) and (b). I assign the absorptivity by a piecewise linear model (see Figure 3.27) in the range from 0 to 0.8 mm. A constant absorptivity (0.41) is assigned to the rest of the scan vector. I apply this simplified model to Case 01. The results are shown in Figure 3.26. The dynamic laser absorptivity model not only results in a better overall prediction of the melt pool length but also reproduces the "bump" seen at the beginning of the scan (see Figure 3.27). A more accurate laser absorptivity that is based on physical testings and models the keyhole behaviors in stages (c) and (d) is outside the scope of the current discussion and will be studied as part of future work to further improve the CAPL approach.

The second future improvement is to better predict the melt pool width as well as the shape of the melt pool. Recent progress in machine learning has enabled an exponential increase in research into leveraging machine learning to predict and control additive manufacturing processes [64, 65, 66]. We developed a conditional Generative Adversarial Network (cGAN) -based approach [67, 68, 69] to predict the melt pool image based on the thermal history along the laser scan path [70]. GAN uses its generator to generate candidates and uses its discriminator to evaluate the candidates. The generator and the discriminator are trained so that eventually the generator is able to predict accurate melt pool frames. The data pair of thermal history and melt pool images for neural network training and validation are obtained through CAPL and AMMT data, respectively (see Figure 3.29). Specifically, We snapshotted the thermal history into a series of thermal distribution images that match the field-

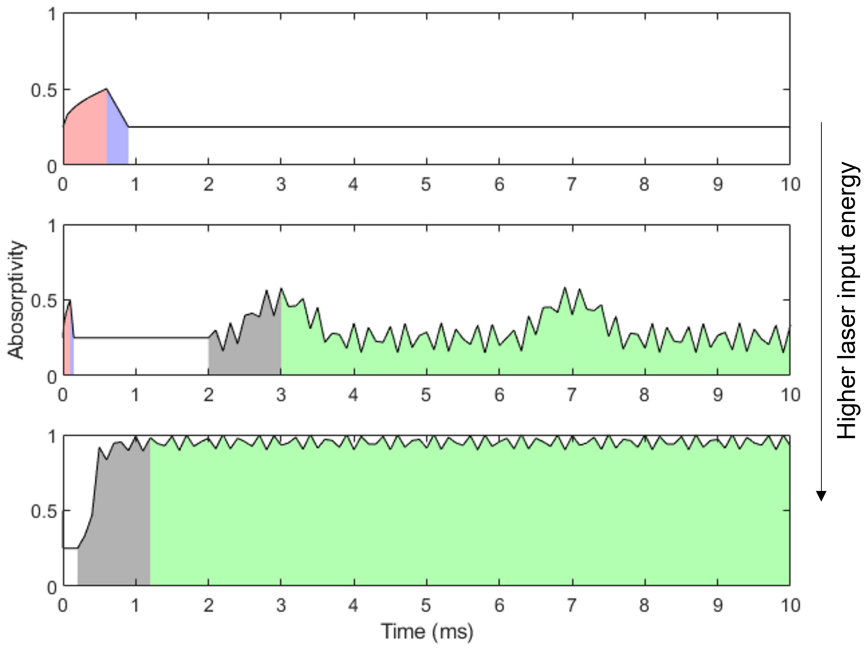

Figure 3.24: A schematic of dynamic laser absorptivity reproduced from paper [3]. The top, middle, and bottom are the dynamic absorptivity under the conduction model, transition model, and keyhole model. The different models are determined by the laser input energy density. Stages (a, in red) and (b, in blue) are mostly visible in the conduction model, while in keyhole model is dominated by stages (c, in black) and (d, in green). In the transition model, all four stages are visible and there is low-frequency keyhole oscillation.

of-view and time steps of the captured melt pool images to work as the conditional inputs into the cGAN. Compared to the interpolation approach discussed in Section 3.3, the machine learning-based approach better captures the overall shape of the melt pool, which, in turn, provides further insight into the steep thermal gradient inside the melt pool. We validated the prediction of the melt pool images through geometric characteristics, including length, width, and angle, of the melt pool. Such a machine learning model could be used to improve the modified conduction model

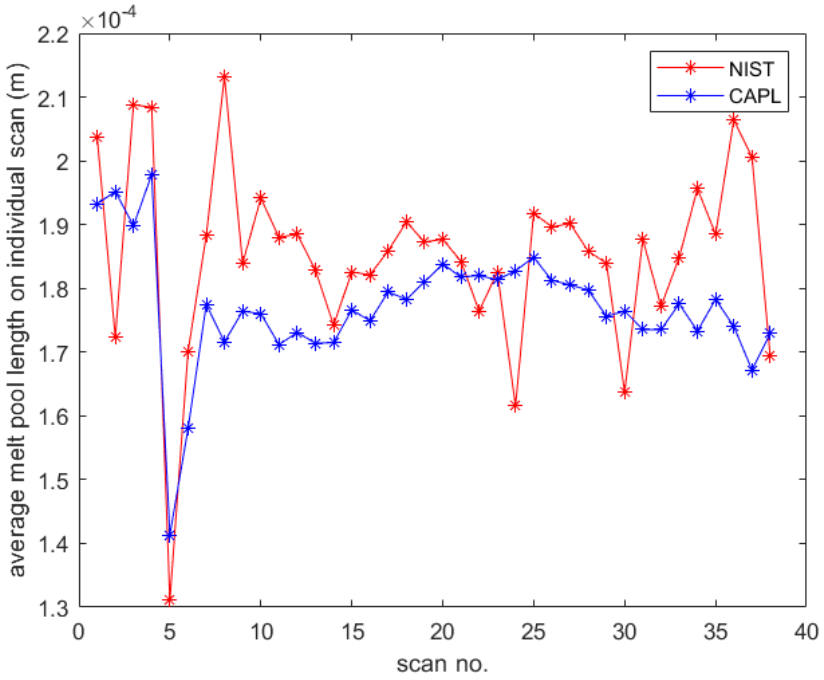

Figure 3.25: Scan-wise average melt pool length, Case 09. Relatively large errors are observed at around Scan 05 and Scan 39, where high laser power is used.

in the present chapter. For example, here the conduction characteristic distance d_0 is a constant, and its machine learning model could be used to map this quantity as a function of process parameters to further improve accuracy.

Simulation of the LPBF process is challenging not only because of the underlying multiphysics and multiscale problems but also the need for calibration due to the intrinsic high uncertainties of many process parameters and material properties. However, the need for recalibration also depends on the particular application of the thermal history result. For example, in the present work, I calibrated the absorptivity since it has a significant influence on the melt pool length. On the other hand, in applications where only qualitative information is required, such as improving the

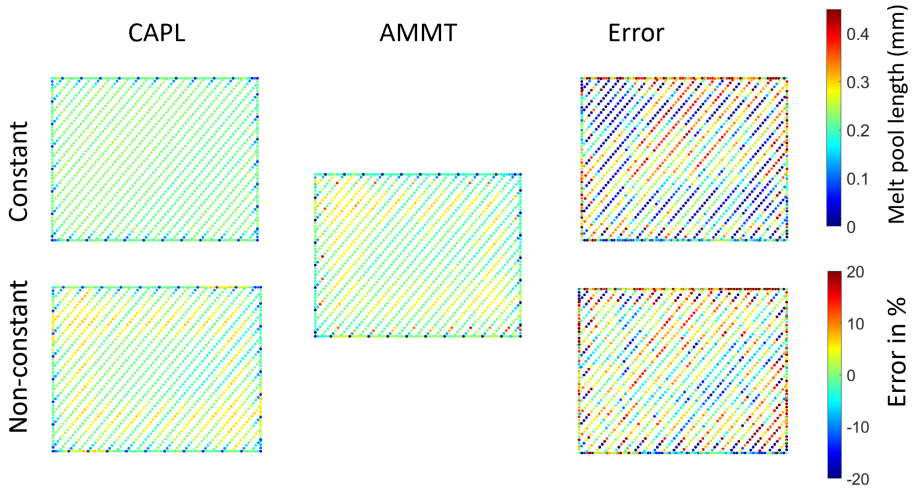

Figure 3.26: CAPL results of Case 01 with the non-constant absorptivity surrogate model (higher absorptivity at beginning of every scan) on the bottom and the results with constant absorptivity on top. Mean error is smaller (9.10%) compared with no surrogate model (11.11%) shown in table 3.2. The underestimation of the "bump" can be seen improved with the non-constant model.

design to reduce over and underheating and using thermal history as a physical prior for machine learning-based melt pool prediction, (re)calibration may not be required.

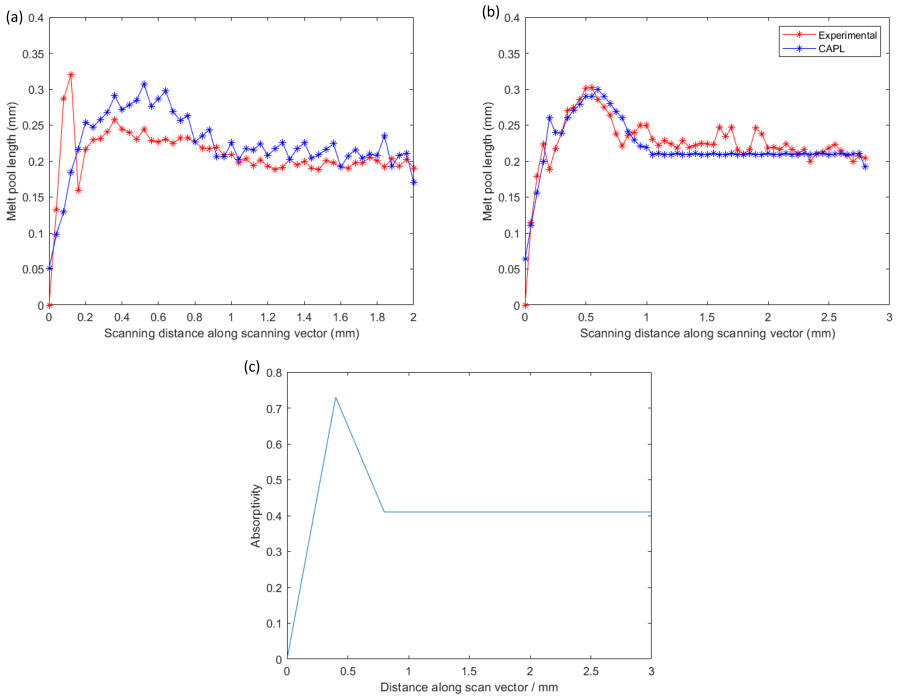

Figure 3.27: CAPL results of Case 01 with the surrogate model of Scan 01 (a) and Scan 19 (b). The "bump" can be reproduced by the piecewise linear surrogate absorptivity model (c). The peak value of the surrogate model is 0.73.

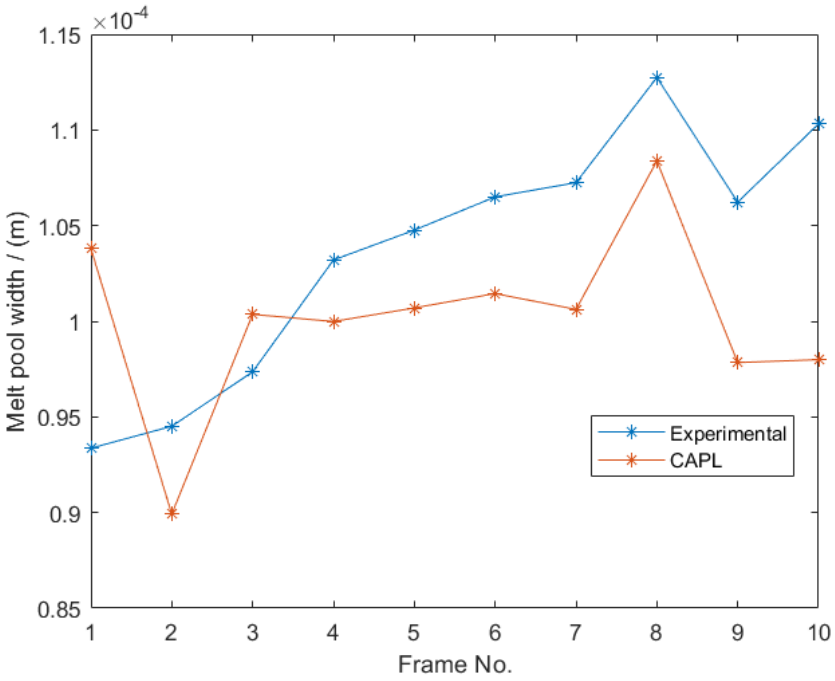

Figure 3.28: Average of melt pool width of Scan 01, Case 01-Case 10.

Figure 3.29: An example of melt pool prediction by machine learning. The left, middle, and right are the input, ground truth, and prediction respectively.

4 PATH-LEVEL RESIDUAL STRESS SIMULATION

4.1 Introduction

Laser Powder Bed Fusion (LPBF) is a form of metal additive manufacturing (AM) that employs lasers as moving heat sources to melt and solidify thin layers of metal powder along a predefined tool path, building the part layer by layer [5, 6, 7]. LPBF has gained significant attention due to its ability to create lightweight, intricate structures. Despite its potential, the full exploitation of LPBF is hindered by the challenge of consistently predicting and controlling the quality of manufactured components and material performance [51]. Complex thermal-mechanical processes give rise to uncertainties such as undesirable deformations, material property variations, and residual stress, which pose significant problems, especially in industries where reliability and precision are paramount. The inability to accurately predict and mitigate these issues has restricted the application of AM in critical areas. The complexity is compounded by scanning paths, as different paths lead to distinct thermal histories and residual stresses, emphasizing the need to understand their influence on material properties.

The LPBF process involves many complex multi-physics and multi-phase phenomena, including the melting of metal powders and remelting of solidified metal, the fluid dynamics and heat transfer of the molten metal, and the microscopic grain structure resulting from the solidification of liquid metals, and so on. Capturing all these effects from the first principle can be extremely computationally expensive, even if only for a small domain. For example, it takes up to 4000 minutes to simulate

a single scan melt pool on a $390 \times 210 \times 50 \mu m^3$ domain [26]. As discussed previously, to simulate the LPBF residual stress, researchers made various assumptions to simplify the model which leads to the "voxel-based approach". Despite the assumptions and simplifications, the voxel-based approach is still expensive and so far is only applicable to a small domain. For example, the simulation of a single layer whose size is 2 mm by 2 mm in the literature takes more than 1 day [41].

To efficiently simulate the residual stress, researchers proposed agglomeration approaches such as the inherent strain method [48, 49] that completely bypass the laser scanning path. This method is a two-step approach. Firstly a full-scale simulation is conducted on a small sample domain to extract the effective “inherent strain”. Then, multiple powder layers are agglomerated as a single “superlayer” where the simulation is conducted as a superlayer-wise activation process. The inherent strain is applied on each superlayer sequentially. This agglomeration approach is very efficient, however, it can no longer predict the effect of the scanning paths. The correlation between the thermal history and the scanning path especially the sequence of melting and solidification is ignored. This is particularly problematic for the boundary region of a layer, as well as layers with intricate details, where the influence of the scanning path is more pronounced.

In the previous chapter, I discussed the PBF-CAPL which captures the thermal histories of the LPBF process [71] on the path level. This approach efficiently captures the influence of the scanning paths on the thermal history. PBF-CAPL differs from the conventional finite element approaches as PBF-CAPL only requires discretization on the path level. The discretized elements of PBF-CAPL are some line segments along

the scanning path. A lumped model is defined on such line segments to model the convection-conduction-radiation problem. I validated this approach by comparing the experimental and simulation melt pool length.

Multiple studies [2, 33, 72, 73] suggested that the residual stress in the LPBF layer is anisotropic: the stress is more dominant in the laser scanning direction than the transverse direction in the powder layer plane. I will use the term "anisotropic stress" of the LPBF process for simplicity. Such anisotropic stress is due to the thermal gradient (spatial temperature gradient) around the melt pool being highly anisotropic [2]. Because the PBF-CAPL uses the lumped element along the scanning path, it does not capture such anisotropic thermal gradients on the path scale. Consequently, PBF-CAPL results can not be applied directly to the conventional finite element-based mechanical simulations.

In this chapter, I developed a novel thermomechanical simulation approach for LPBF based on the path-level thermal history. The new approach requires a coarser discretization compared to those used in conventional voxel-based approaches. An overview of the new approach is shown in Figure 4.1. Firstly I computed the residual stress of around the steady-state melt pool from a fine-scale simulation to capture the anisotropic stresses. Secondly, I used a path-level thermal simulation to obtain the thermal history for the given scanning path. Then I utilized the fine-scale results and the path-level thermal history to compute an "effective thermal strain" which reflects the anisotropic stresses. The effective thermal strain is an anisotropic strain that is to be used in the path-level mechanical simulation. Lastly, the effective thermal strain is applied to the path-level mechanical simulation to simulate the LPBF path-level

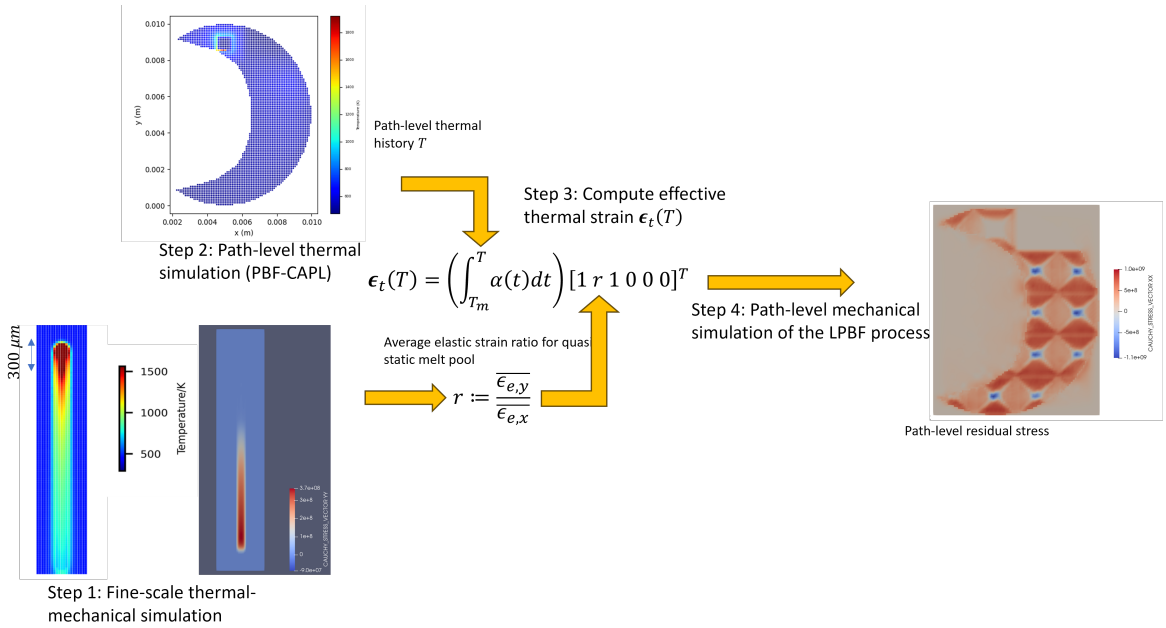

Figure 4.1: Outline of the path-level LPBF simulation

residual stress.

My main contribution is to provide an approach to simulate the residual stress on the path level. I developed this new approach with an effective thermal strain used to address the anisotropic stresses in the scanning and transverse directions. The new approach is more efficient compared with the conventional voxel-based approach which requires the discretization to capture the details of the melt pool. The discretization used in the proposed approach only needs to capture the scanning paths. Thanks to the better efficiency, I can simulate the LPBF scanning process on larger and more complex layers. I further investigated the effects of layer shapes and scanning paths on the residual stress. To the best of the authors' knowledge, little work has been done to investigate the influence of the laser scanning path especially

the sequence of the melting and solidification on the residual stress using simulations.

The rest of the chapter is organized as follows. In Section 2, I will formulate and validate a new path-level mechanical simulation framework for the LPBF process. In Section 3, I will present the simulation results of different island checkerboard patterns, including single island tests and single layer tests which include multiple full or trimmed islands. I will discuss the effect of the scanning path on the path-level residual stress based on my simulation results. In the last section, I will conclude the present work and discuss the possible future work.

4.2 Formulation

As discussed previously, voxel-based approach requires fine discretization to capture the thermal gradient around the melt pool. Consequently, the thermal history from PBF-CAPL cannot be directly applied because it lacks the resolution in the transverse direction. In my method, I proposed a novel effective thermal strain to capture the anisotropic stresses. The proposed method includes four major steps: (1) Obtaining the desired anisotropic stress by simulating the residual stress of around a melt pool using the conventional voxel-based approach. (2) Conducting path-level thermal simulation by PBF-CAPL. (3) Constructing the effective thermal strain with the thermal history from the PBF-CAPL and the anisotropic stress from the voxel-based approach. (4) Conducting the path-level mechanical simulation by applying the effective thermal strain. I will show the details below with an example compared to the results by the voxel-based approach [2].

In the first step, I conducted the thermomechanical simulation of a steady-state

Table 4.1: Process parameters and material properties of Ti6Al4V [2]

Melting temperature	1923 K
Environmental temperature	473 K
Layer thickness	40 μm
Laser power	82.5 W
Laser speed	0.5 m/s
Environmental convection coefficient	10 W/(m^2 K)
Element size	20 μm
Laser spot size	50 μm

melt pool to obtain the residual stress distribution with the voxel-based approach. This step serves the purpose to obtain the ratio of the anisotropic stresses in the scanning and the transverse direction, which will be used to compute the effective thermal strain in the following steps. I chose the scanning path length to be 3 mm to ensure a quasi-steady state is reached. The simulation use the weakly coupled voxel-based simulation. The thermal simulation is implemented with a homemade finite element code. The simulation and process parameters are given in table 4.1. The mechanical simulation is implemented with the KratoMultiphysics [74, 75, 76]. The melt pool temperature distribution and the stress are shown in Figure 4.3.

The second step is to obtain the path-level thermal history. The thermal history, along with the ratio of the residual stress from the previous step, will be used to compute the effective thermal strain. I used PBF-CAPL to compute the path-level thermal history. The scanning paths are given in Figure 4.2 and the process parameters are given in Figure 4.1.

The third step is to compute the effective thermal strain. In this step, I converted the results of the fine-scale problem into a model to be used in the path-level problem. Recall the purpose of the effective thermal strain is to reproduce the same anisotropic stresses. For the fine-scale problem, the residual stress comes from the anisotropic

thermal gradient which causes non-uniform deformation around the melt pool. The deformation in the path-level simulation is more uniform since one path-level element covers the entire hatching space. To achieve the same anisotropic stresses, we alter the thermal strain on the path level from the conventional isotropic one to an effective anisotropic one (assuming scanning along x direction):

$$\boldsymbol{\epsilon_{t,e}}(T) = (\int_{T_m}^{T} \alpha(t)dt)[1, r, 1, 0, 0, 0]^T \tag{4.1}$$

where r leads to the anisotropic stresses. Now the question becomes how to determine r. Note deformation and plasticity happen mostly when temperature is high (stiffness is low) and stresses build up after cooling down. When stresses build up, I considered the deformation of the path-level element to be approximated to the plastic deformation, therefore $\epsilon_e + \epsilon_t = \epsilon_{total} - \epsilon_p = 0$, then by Hooke's law we have the following equation for a path-level element:

$$r = \frac{\epsilon_{t,x}}{\epsilon_{t,y}} = \frac{\epsilon_{e,x}}{\epsilon_{e,y}} = \frac{1/E(\sigma_x - \nu\sigma_y)}{1/E(\sigma_y - \nu\sigma_x)} = \frac{1 - \nu\frac{\sigma_y}{\sigma_x}}{\frac{\sigma_y}{\sigma_x} - \nu} \tag{4.2}$$

Because we need to ensure the same anisotropic stresses, the ratio $\frac{\sigma_y}{\sigma_x}$ needs to be equal to the one from the fine-scale problem. The corresponding value in the fine-scale problem is the ratio of the average stresses of the stress distributions around the melt pool $\frac{\bar{\sigma}_y}{\bar{\sigma}_x}$. Now r is available when we substitute $\frac{\bar{\sigma}_y}{\bar{\sigma}_x} = \frac{\sigma_y}{\sigma_x}$ into equation 4.2. Then we have the expression of the effective thermal strain in equation 4.1: its coefficient $\int_{T_m}^{T} \alpha(t)dt$ reflects the thermal history while the value r causes the anisotropic stresses. The average residual stress is computed by taking all the elements' stress except for those

whose magnitude is smaller than ϵ. The exclusion of these elements is to exclude the non-melted elements. In the current chapter I chose $\epsilon = 1$ KPa. The average residual stress is computed as $\bar{\sigma_x} = 61$ MPa, $\bar{\sigma_y} = 30$MPa, so we have the ratio $r = 0.2$ according to equation 4.2 and the effective thermal strain $\boldsymbol{\epsilon_{t,e}}(T) = (\int_{T_m}^{T} \alpha(t)dt)[1, 0.2, 1, 0, 0, 0]^T$.

The last step is to apply the effective thermal strain in the path-level simulation. The path-level simulation use the same implementation as the conventional voxel-based approach except for two differences: (a) The thermal strain will be replaced by the effective thermal strain, and (b) the domain is discretized to capture the scanning path (instead of fine discretization to capture the melt pool).

Because we use the effective thermal strain and it is no longer needed to capture the details of the melt pool shape, the discretization is only needed to capture the scanning path instead of the melt pool shape. In my thermal simulation using PBF-CAPL, the discretization is linked to the scanning path, with the path-level elements having their widths set equal to the hatch space. In the mechanical simulation, the discretization is needed to capture the same scanning path. For simplicity, I used a regular voxel mesh whose element size is the hatch space since such a discretization is enough to capture the scanning path. The temperature of the mechanical element is mapped from the nearest thermal element. Compared to the conventional approaches, both my thermal and mechanical simulations have a much coarser discretization and thus are more computationally efficient. It is noteworthy that we can alternatively reconstruct the melt pool shape directly from path-level thermal history using our MeltpoolGAN [70]. This fast reconstruction method enhances efficiency and better accounts for the variations in melt pool shape under different combinations of laser

speed and power compared to the thermomechanical simulation.

I compared the path-level simulation results with the results of voxel-based approach from literature [2]. The scanning of a single-layer Ti6Al4V powder is simulated. Scanning paths include a post-contour scanning of (a) unidirectional parallel scanning and (b) alternating parallel scanning. I conducted the path-level simulation of the same paths with my new proposed approach. As discussed previously, my approach only needs discretization resolution to capture the scanning paths, the element size is small as long as it is comparable to the PBF-CAPL element. Here, the element size is $90 \times 100 \times 40\ mm^3$ (in the reference paper the element size is $20 \times 20 \times 20\ mm^3$). It can be seen my approach uses much fewer elements ($20 \times 20 \times 20 : 90 \times 100 \times 40 = 1 : 45$).

The results show that my approach is a good match compared to the voxel-based approach. It is noted by the researcher that there are three scanning-path-led patterns [2]: (a) the "ripple effect" is found in the stress distribution, (b) stress is situated centrally along the hatch region and decreases toward the end of the scan vectors in the hatched region, and (c) the stress in the scanning direction is more dominant compared to those in the transverse direction. As shown in Figure 4.4, all these three patterns are replicated by my path-level simulation. The maximum magnitude of the stresses also approximately matches the results from the literature. The slight difference between these numbers might come from different physics models. For example, the preclusion of latent heat in the reference implementation lead to abnormally high maximum temperature. The inclusion of latent heat in PBF-CAPL significantly decrease in the maximal temperature into the normal range, result in a quantitatively different stress than the reference implementation.

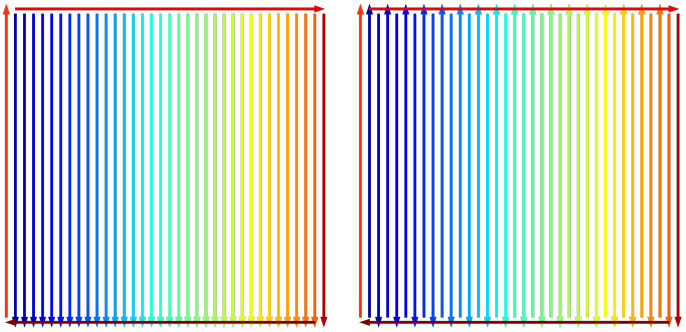

Figure 4.2: Scanning paths (unidirectional and alternating with a contour scanning) used by Parry et al. [2]. The laser start from blue to red. As shown by the color, the post contour scanning happens after the parallel scanning.

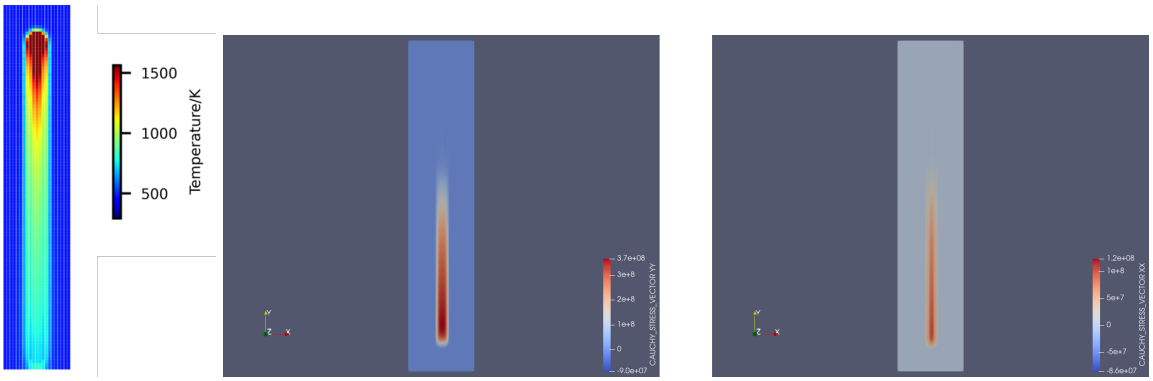

Figure 4.3: Snapshot of temperature distribution around the melt pool and the fine scale residual stress. The pixel size is 20 μm. The melt pool length is 0.32 mm. Left: stress along the scanning direction. Right: stress in the transverse direction.

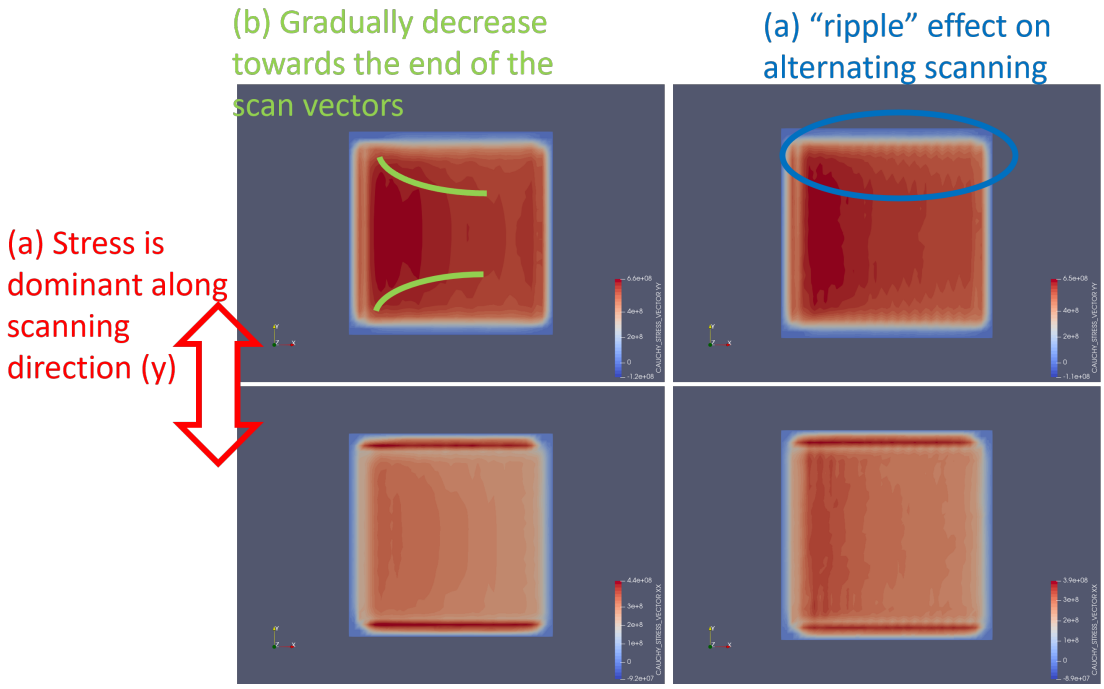

Figure 4.4: Simulation results by my approach (unidirectional at left and alternating at right). The top is the stress in y direction and the bottom is the stress in x direction.

I further demonstrated that my approach is indeed reasonable by comparing it to the key parameters used in the inherent strain method [48]. The cross-validation results are available in another paper [48], where the authors obtains the inherent strain for Ti6Al4V is determined as $\epsilon_x = 0.013$ and $\epsilon_y = 0.003$. If we consider thermal history to be uniform with constant r, then my approach can be described as the inherent strain method on the path level. Considering the thermal expansion coefficient is around the order of $10^-5/K$ and the melting point for the metal is around 1923 K, the thermal strain (cooling down from melting point to room temperature) can be estimated as $(1923 - 293)K * 10^-5/K = 0.0163$, which is approximated to the order of 0.013 given by the literature. Recalling we have the ratio $r = 0.2$, the inherent strain

is estimated to be $\epsilon_x = 0.0163$ and $\epsilon_y = 0.0163 * 0.2 = 0.00326$, which is a good match with the results from the literature $\epsilon_y = 0.003$.

I further demonstrated that my approach is indeed reasonable by comparing it to the key parameters used in the inherent strain method [48]. . Cross-validation results can be found in another paper [48], where the inherent strain for Ti6Al4V is determined as $\epsilon_x = 0.013$ and $\epsilon_y = 0.003$.

If we assume the thermal history to be uniform with a constant r, my approach can be conceptualized as the inherent strain method at the path level. Considering the thermal expansion coefficient is approximately $10^{-5}/K$ and the melting point of the metal is around 1923 K, the thermal strain (cooling from the melting point to room temperature) can be estimated as $(1923 - 293)K \times 10^{-5}/K = 0.0163$. This is approximately equivalent to the value of 0.013 given in the literature. Taking into account my ratio $r = 0.2$, the inherent strain is estimated to be $\epsilon_x = 0.0163$ and $\epsilon_y = 0.0163 \times 0.2 = 0.00326$. This estimation aligns well with the literature value of $\epsilon_y = 0.003$.

4.3 Residual stresses on island patterns

In this section, I will simulate the residual stresses of various island checkerboard patterns. I will first conduct simulations of single islands as well as single layers that consist of multiple full and trimmed islands. I will then discuss the influence of path-level thermal history and the layer boundaries on the residual stress with the simulation results. I observed two factors that affect the path-level residual stress: one is the the uneven shrinkage caused by the order of solidification, another is the

Table 4.2: Process parameters for island tests.

Environmental temperature	473 K
Absorptivity	0.77
Hatch space	100 μ m
Layer thickness	40 μ m
Laser power	80 W
Laser speed	1 m/s
Environmental convection coefficient	10 W/(m^2 K)
Laser spot diameter	50 μm
Platform thickness	4 mm

thermal history more specifically the cooling rate.

Residual stresses on various single-island pattern

Island patterns are increasingly popular for the LPBF scanning paths [77, 78]. In this chapter, scanning patterns including unidirectional scanning, checkerboard patterns, and spiral patterns are simulated as single-layer tests, shown in Figure 4.3. The color from blue to red represents the laser start and end positions. I used the same process parameters for all the patterns, see table 4.2. All the patterns have the same 2 mm $\times$ 2 mm dimension.

The residual stress shown in Figure 4.3 are those when the layer is cooling down to environmental temperature. The simulation results show that the residual stress at a specific point is mostly dominated by the scanning direction through the specific point except for some regions in two cases: the inward spiral case and the pre-contour case. In most cases, the residual stress is tensile (positive) as the consequence of the volume is shrinking due to cooling: the materials tend to shrink, but the shrinking tendency is constrained by its neighbor. In other words, a specific point is stretched by its neighborhood, therefore the stress is tensile. However, there are compressive

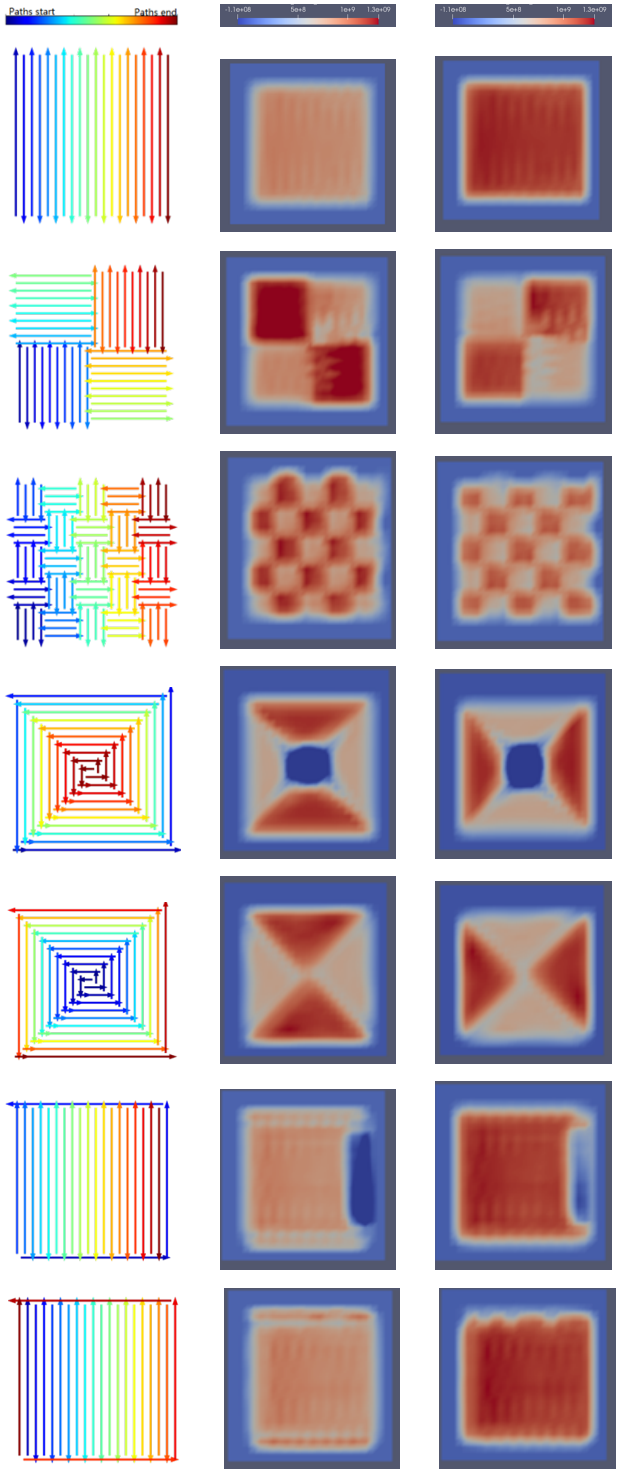

Table 4.3: Table of single island residual stress (Pa).

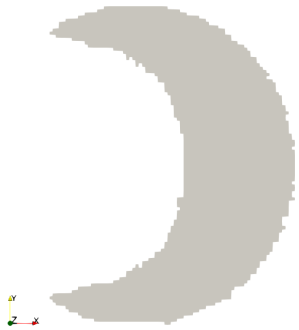

Figure 4.5: The crescent moon shape of the single layer simulation.

stress regions in the pre-contour and the inward spiral cases. In both two cases, the compressive regions are the last region to be scanned and solidified. The compressive stress is likely due to the already solidified neighborhoods which act as constraints that limit the deformation of the last region in all directions. Though the last region intends to shrink, it has expanded in the transverse direction due to the Poisson effect. Such expansive deformation is limited by the neighborhood which causes strong compression.

Residual stresses on multiple trimmed islands

I simulated the LPBF process on a larger crescent moon shape which contains multiple full and trimmed islands. As shown in Figure 4.5, the scanning on a crescent moon of 8 mm $\times$ 10 mm is simulated. The process parameters are the same as those used in the single-island simulation.

I tested my simulation approach on various island patterns. The simulation results indicate that the residual stress patterns generally resemble those from single island

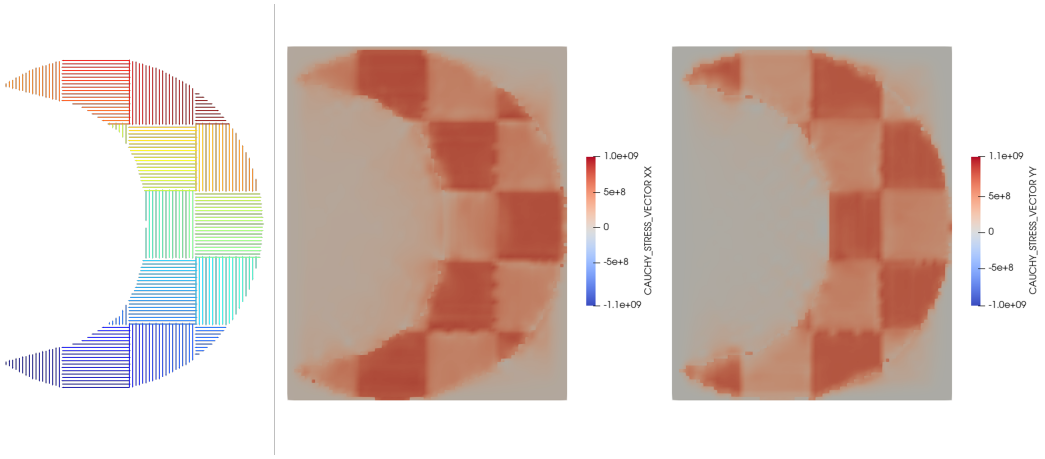

Figure 4.6: The Cauchy residual stress in XX and YY directions of an alternating parallel islands crescent moon.

tests. As shown in Figures 4.6 and 4.7, the results of most spiral islands are similar to the one in the single island test, except for the left bottom corner one in the red box. The compressive region is barely visible in the red box. I postulated the reason for this difference is that the center of the island is no longer constrained by its neighborhood in all directions since part of the island is trimmed off. Again, this case shows how the scanning order and the layer shape can affect the residual stress.

It is noteworthy that most of my islands have similar residual stress as those in the single-island tests. Note that $\epsilon_{total} = \epsilon_e + \epsilon_t + \epsilon_p$, such similarity suggests for those islands, their ϵ_{total} and ϵ_t are similar those on the other islands respectively. This similarity of ϵ_{total} is attributed to the fact that the deformation is small in the single-layer test. In the single-layer test, the layer is fully attached to the platform as there is no underlying overhang region, therefore deformation is expected to be small. In general cases, small deformation is expected in the absence of overhangs or when overhangs are present but adequately supported. The similarity of ϵ_t indicates

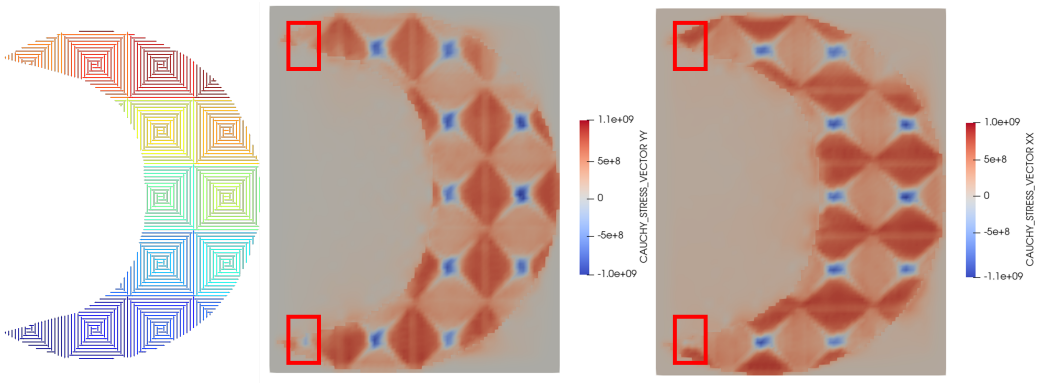

Figure 4.7: The Cauchy residual stress in XX and YY directions of an spiral islands crescent moon. The compressive region in the red boxes are not clearly visible due to they are on the layer shape boundary.

the thermal history is similar on different islands because of the rapid cooling and solidification as the layer is fully connected to the underlying platform. Figure 4.8 demonstrates the stress in one island rapidly builds up as the laser moves away from this island: as the laser is scanning in the island at $x \in [0.004, 0.006], y \in [0.008, 0.01]$ mm, the temperatures are elevated and stress levels are low. Temperature rapidly decrease to below 1000 K and the stress increases in regions where the laser moves away from these areas.

Such highly localized stress formation results in similar stress distributions across different islands with the same pattern. Despite their similarity, the influence of heat accumulation on stress, resulting from the scanning paths, remains noticeable. I demonstrated such difference in Figures 4.9 -4.11. I used the time over threshold temperature [79] to demonstrate the difference of thermal histories. Here I chose the threshold to be 923 K. It shows that the thermal history varies among different islands based on their order, owing to differences in thermal accumulation. The time over

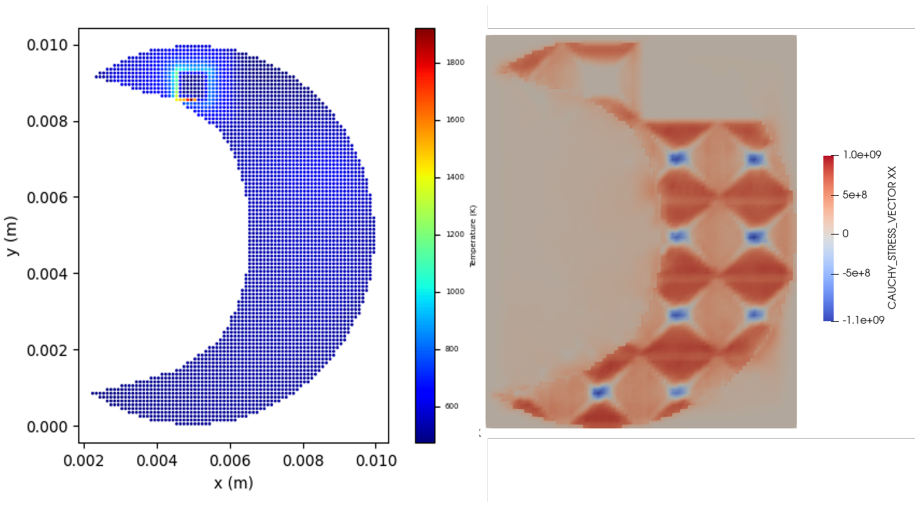

Figure 4.8: The residual stress and the temperature during the scanning process.

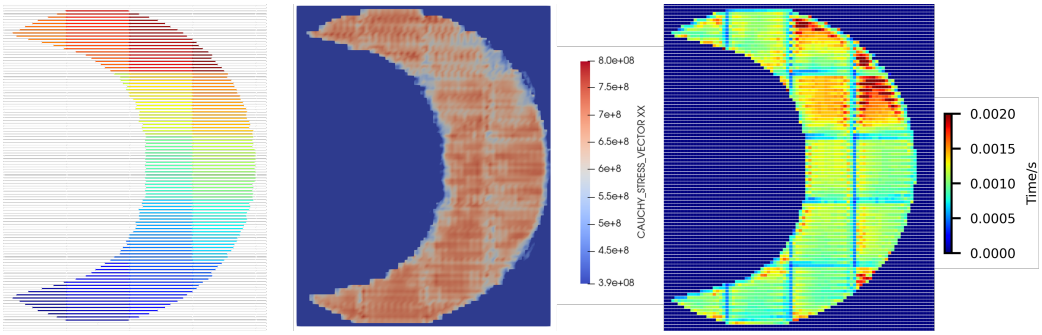

Figure 4.9: The residual stress and the time over threshold of parallel scanning paths.

threshold is larger for the islands that are scanned after their neighboring islands, compared to those scanned earlier in the sequence. In other words, the cooling for these islands are slower. Compared with the stress distribution, it is shown that the low residual stress regions coincide with the region having a higher time over threshold. This indicate the slow slow cooling is likely to cause less residual stress. These cases show how the sequence of islands can affect the cooling rate which causes different residual stress distribution.

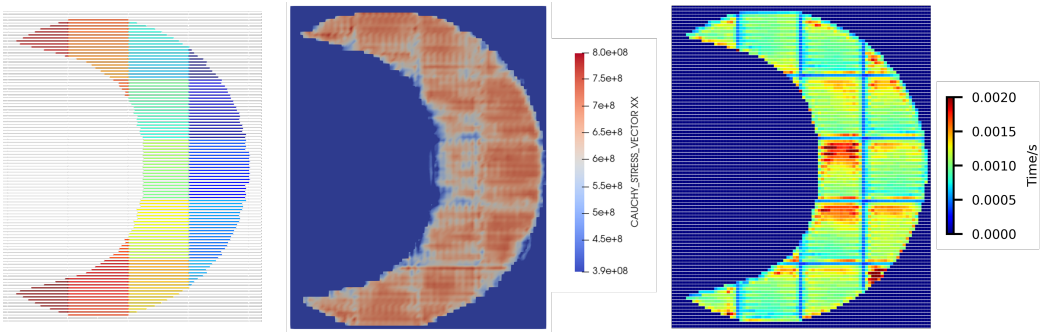

Figure 4.10: The residual stress and the time over threshold of parallel scanning paths in the reverse order of the case in Figure 4.9.

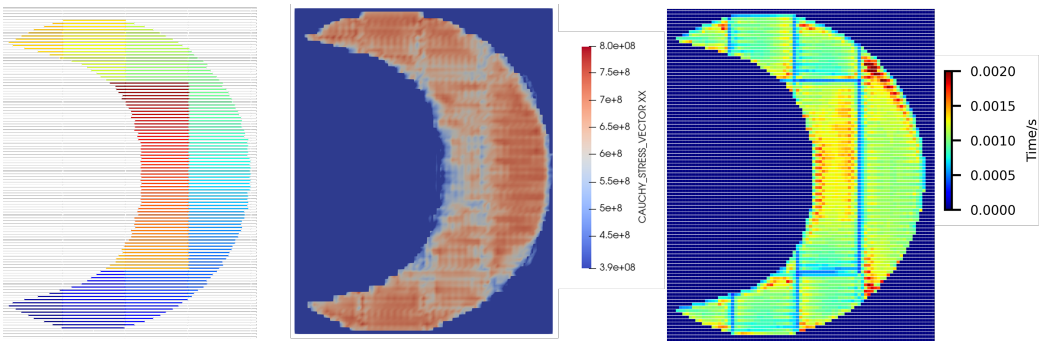

Figure 4.11: The residual stress and the time over threshold of parallel scanning paths in the spiral order of the case in Figure 4.9.

4.4 Discussion

In this chapter, I proposed an approach to simulate the residual stress on the path level. The proposed approach is capable to utilize the path-level thermal history to simulate the residual stress. The proposed approach is capable of capturing the path-level thermal and mechanical evolution. Compared with existing approaches, the present approach is more accurate than the layer-based approach since it is capable to simulate on the path level, and it is more efficient than the conventional voxel-based approaches

as the new approach does not need to capture the details of the melt pool. I validated my present approach by comparing my simulation results with the results by the voxel-based approach from the literature. A good match is obtained. I discussed the factors that affect the residual stress by conducting numerical simulations with my approach to the island's patterns. The influence of the path-level thermal history and the layer shape on the residual stress are discussed.

Understanding the gaps in existing methods is crucial for advancing the simulation of LPBF processes. Currently, available approaches provide efficient layer-wise methods like the inherent strain method, along with accurate but more expensive voxel-based approaches. While the efficient layerwise methods excel in regions where the path is less significant, identifying the regions where the path plays a crucial role and determining how to address them remain challenges. It is imperative to comprehend the assumptions or process parameters that dictate the efficacy of these methods.

The stress observations from my study shed light on these challenges. I found that the stress in the single-island test closely resembles that of the multi-island layer. This similarity might be attributed to the localized formation of residual stress, a result of rapid cooling and minimal deformation in the single-layer test. I demonstrated that my approach can be simplified to a path-level inherent strain method with these observation assumed. However, I also highlighted that stress can be influenced by the complex layer boundary and the sequence of solidification.

Incorporating path-level stress simulation and the path-level thermal simulation could be a pivotal component of a comprehensive part-scale LPBF simulation strategy.

I developed a hybrid layer-path thermal simulation approach which will be discussed later. The path-level simulation is conducted at the region where the scanning path has critical influence. The mechanical simulation methodology introduced in this chapter could potentially serve as a foundation for a comparable layer-path mechanical simulation, bridging the identified gaps in existing methods.

5 MULTISCALE SIMULATION

5.1 Introduction

While the LPBF process holds immense promise for advancing manufacturing capabilities, the optimization of process parameters and the prediction of final part quality remain significant challenges due to the complex thermal history. The complex thermal history directly influences the microstructure [15], mechanical properties [16, 17], and overall performance of the final part. The localized heating and rapid cooling inherent in the LPBF process introduce complexities that necessitate a nuanced understanding of the process dynamics. The aim of modeling these processes is to gain input into process behaviors and confidence in process configurations. Researchers have explored voxel-based approaches for simulating LPBF processes as discussed previously. Voxel-based simulations offer high fidelity in capturing the thermal history and material behavior along individual scanning paths. However, they often suffer from prohibitively high computational costs [80, 81], limiting their practical applicability for process optimization and part quality prediction. Recognizing the computational challenges, researchers have proposed layer-based approaches, where each layer is treated as a homogeneous entity subjected to uniform thermal conditions. While layer-based simulations offer computational efficiency, they sacrifice the ability to address path-level issues and accurately represent the non-uniform thermal profiles experienced by individual scanning paths. The loss of path-level information in thermal history might cause unexpected warping, residual stress, or deviations in the material properties [51, 52]. Insight into scan strategies, when accompanied

by the necessary controls, can be used to reduce residual stresses and even create tailored microstructures. The better a model can capture the complex physics, the greater the chances of achieving desired outcomes. The faster the model can compute solutions, the more practical and efficient it is for adoption, particularly when aiming to achieve part scales.

A common trade-off encountered when modeling AM processes is one of fidelity versus performance. A delicate balance is often desired when accounting for these two factors, especially when exploring real-time and near-real-time applications. In the previous work, I developed a path-level simulation approach called PBF-CAPL [82]. The PBF-CAPL addresses the shortcomings of both voxel-based and layer-based approaches by offering a scalable solution that captures the path-level dynamics of LPBF while maintaining computational efficiency. I have validated my approach on an Inconel 625 (IN625) bare plate with the melt pool length coming from the melt pool images by National Institute of Standards and Technology (NIST) Additive Manufacturing Metrology Testbed (AMMT) data [56]. Though PBF-CAPL is scalable, substantial amount of timestep are required for a part-scale problem.

Though the PBF-CAPL is more efficient compared to the voxel-based approach, it is still challenging to simulate the part-scale problem due to the large number of timesteps which is required. In the present paper, I proposed a novel simulation approach that integrates both path-level and layer-level methodologies to enhance efficiency for the 3D part. This proposed approach is capable of providing a path-level thermal history on 3D structures. I tested my approach on a part built by an LPBF process with IN625 powder [1]. This study will contribute to the deeper comprehension

[1]The data can be downloaded from NIST [83]

of the LPBF process, particularly concerning phenomena associated with scanning paths and their impact on 3D features, such as overhangs.

5.2 Formulation

Hybrid layer-path approach

In the proposed new approach, I developed an layer-level mode and synergistically integrate the path-level mode and the layer-level mode. The layer-level mode provides a fast simulation of the low-fidelity temperature where the scanning path does not have a significant influence. Then the low-fidelity temperature will be used in the path-level simulation where the thermal history is more path-sensitive.

In the layer-level mode, the heat source, Q_i, is applied on the powder layer i in a short period T_e called exposure time. In a specific location x on a specific layer, the laser input energy $H(x,t)$ is a function of x and time t according to the scanning path. Usually, time t determines the laser location, and $H(x,t)$ is a Gaussian distribution around the laser location at time t. The heat input equals the integration of the laser heat energy along the scanning paths on the layer:

$$Q_i(x) = \int_{t_0}^{t_1} H(x,t)dt \tag{5.1}$$

where the t_0 is the time x being melted and t_1 is the time when the laser is deactivated in the current layer. This formulation considers the influence of remelting by the laser input energy after the melting time t_0. Then the heat source Q_i is computable as a distribution (a function of x) on the layer i.

It is noteworthy that the exposure time is a critical parameter governing the thermal history in the layer-level approach. A shorter exposure time will lead to higher temperatures because the heat conducted away is less in a shorter period. In this study, I calibrated the exposure time to be 5×10^{-5} seconds. Here the calibration of the exposure time is to ensure the thermal history in the lower temperature range is correct so that the low-fidelity thermal history is applicable to the path-level mode. The proposed approach switches from the layer-level mode to the path-based mode when the laser moves close to the region of interest. The temperature from the layer-level mode is used as the initial temperature for the path-level simulation which is discussed in the previous chapter.

Calibration

I used the "Overhang Part X4" dataset from the AMMT at NIST [83]. The original dataset comes from the building of four nominally identical parts. Each part ($5 \times 5 \times 9mm^3$) has two overhang features, one is a cylindrical cutout, and another is a 45° overhang slope, as shown in Figure 5.2. The part consists of 250-layer scanning. The layer thickness is 20 μm. In each layer, the laser first has a contour scan when the power is 100 W and the speed is 0.9 m/s. After the contour scanning, the laser scans the interior region, with the power being 195 W and the speed being 0.8 m/s. The scan direction switches alternatively between 0° and 90° at even and odd layers, respectively. The nominal hatch space is 100 μm and it is slightly adjusted in each layer. Specifically, the path-generation algorithm takes the longest distance of the layer and then divides it evenly to obtain the hatching space.

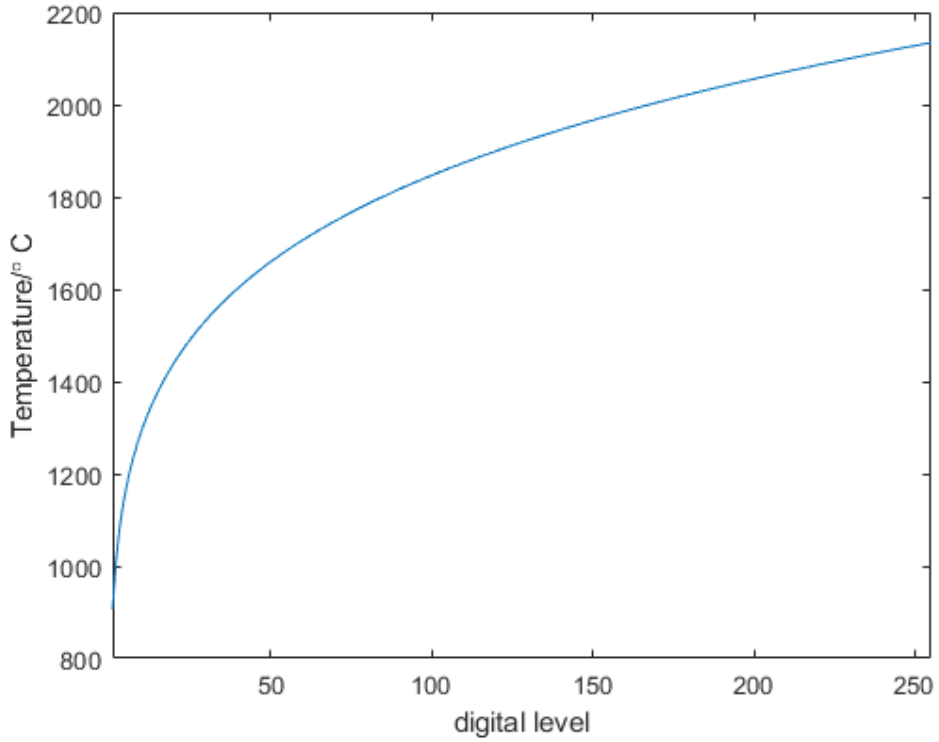

Figure 5.1: The polynomial curve of the relation between temperature and digital level value (1-255).

The dataset is the melt pool images acquired during the execution of the aforementioned process plan by the co-axial melt pool monitoring (MPM) at NIST. The melt pool image is 120 x 120 pixels at a resolution of 8 um/pixel. Each pixel in the melt pool image is an 8-bit digital value, which is calibrated to a function of temperature by the Sakuma-Hattori equation [84]. A fitted polynomial model is $T = aS^b$ where $a = 906.2, b = 0.1546$, see Figure 5.1.

In this section, I calibrated the LPBF process parameters including absorptivity and powder conductivity by measuring the track length over the threshold temper-

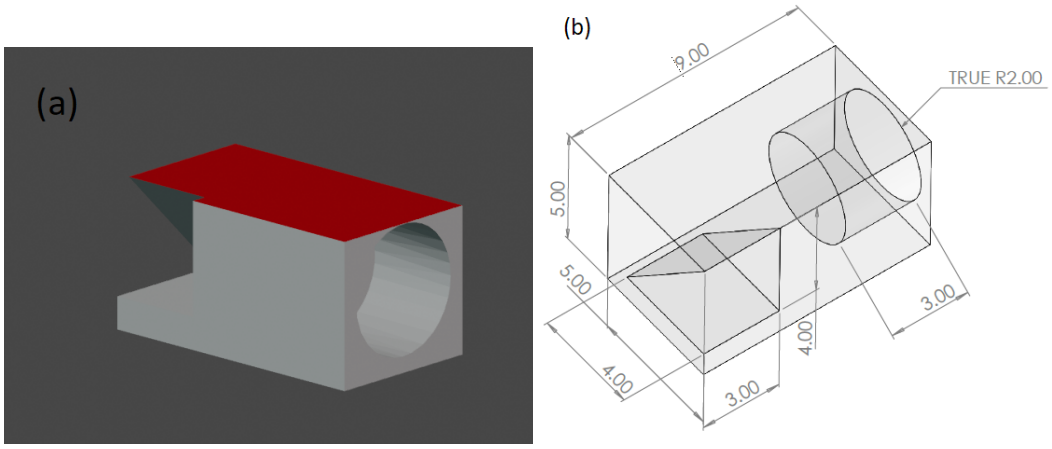

Figure 5.2: (a) The layer 226 (the red cross section) is the layer at the upper end of the cylindrical cutout. (b) The part drawing.

ature. I chose the threshold temperature to be $1800°C$ because I could obtain the corresponding track length from the melt pool images. The melt pool image size in this work is 0.96 mm by 0.96 mm. The track length exceeds the melt pool image size if the threshold is too low, see Figure 5.3. The calibration is performed to optimize the process parameters to achieve a simulated track length that correlates with the experimental data. I simulated one of the four identical parts with my proposed approach, where the layer-level mode is used for layer 1 to layer 209, and the path-level mode is used for layer 210 to layer 226. I then compared the simulation results and the experimental results. I calibrated the absorptivity to be 0.7 and the powder conductivity to be a function of temperature. The process parameters including the calibrated ones are shown in table 5.1.

It's noteworthy that the overhang region exhibits a shorter melt pool length over 1800 °C. Similarly, the time over 1800 °C at the overhang region is also shorter, see Figure 5.4. This might be counter-intuitive: conventional wisdom suggests that the

Table 5.1: Process parameters and IN625 thermal material properties

Process parameters	Values
Absorptivity	0.7
Laser spot size	60 μm
Convection coefficient	15 $W/(m^2K)$
Platform temperature	298 K
layer thickness	20 μm
IN625 density	8440 kg/m^3
IN625 conductivity $k(T)$ $(293K < T < 1563K)$	[(T-293)/63.5+10]$W/(m \cdot K)$
IN625 conductivity $k(T)$ $(T > 1563K)$	30 $W/(m \cdot K)$
IN625 conductivity of $k(T)$ $(T < 293K)$	10 $W/(m \cdot K)$
IN625 Powder conductivity $k_p(T)$	$0.001k(T)$

overhang region is more prone to overheating due to the lower thermal conductivity of the powder. However, experimental data suggests otherwise. Despite the cylinder cutout overhang region and the non-overhang region have the same laser speed and power, the time over thresholds are different. In fact, Zhuo et al. [85] also noticed that the overhang region has the lowest remelting by the neighboring scans. They also noticed that the remelting will only gradually recover in the subsequent layers.

These observations imply that another factor is at play: compared to the melted region, the unmelted powder may remain cooler and serve as a relative cooling source for subsequent layers. Consequently, the powder's conductivity needs to be lower to prevent excessive heating. In the present study, I calibrated the conductivity to 0.1% of the bulk material conductivity.

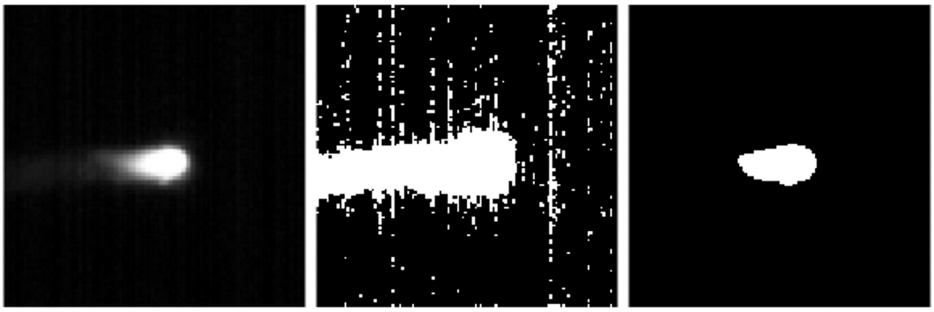

Figure 5.3: Left: Raw melt pool image. Middle: the binarized image with threshold = 7. Right: the binarized image with threshold = 79.

5.3 Analysis of thermal history trends

Time over different threshold temperatures

My simulation results corroborate the features of the overhang region observed at NIST (shown in Figure 5.5). Specifically, at the layer (layer 226) which is just above the cylinder cutout which has the most overhang below, the overhang region exhibits a distinct thermal history compared to the non-overhang regions. The time over threshold from the experimental data (shown in Figure 5.4) is generated by Ho and Brandon's algorithm [79]. Compared to the non-overhang region, the overhang region exhibits a longer time over threshold for lower temperature thresholds. Conversely, the overhang region has a shorter time over threshold for the higher temperature thresholds.

I further noticed that this feature is particularly sensitive to temperature threshold, especially around the melting point. As illustrated in Figure 5.6, the time over threshold is longer at the overhang region at the melting point $1290°C$, but with a little higher threshold, the time over threshold becomes shorter than those at the

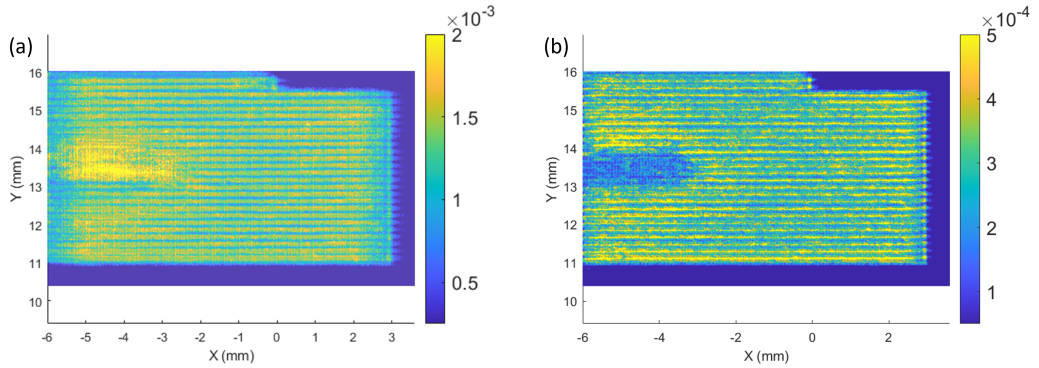

Figure 5.4: (a) The experimental time over threshold in second (threshold = 10). (b) The experimental time over threshold in second (threshold = 79).

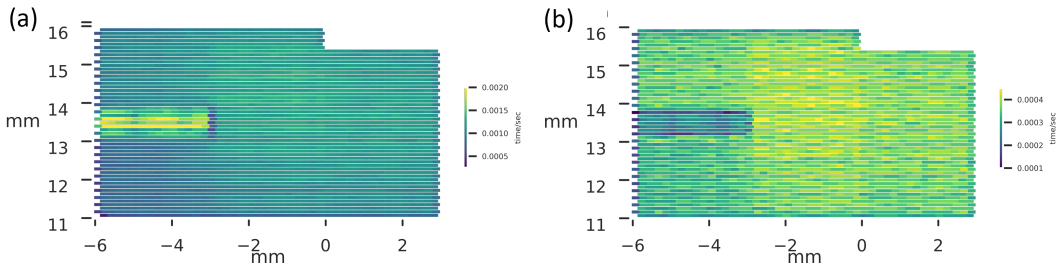

Figure 5.5: (a) The simulation time over threshold in second (1300°C) at layer 226. (b) The simulation time over threshold in second (1800°C) at layer 226.

non-overhang region. I reproduced the same phenomenon by my simulation, as shown in Figure 5.7.

Overall thermal history difference layer by layer

One notable characteristic of the dataset utilized in this study is the absence of thermal accumulation observed layer by layer, contrary to initial expectations. Instead, each layer exhibits a cooling trend as subsequent layers are deposited. As demonstrated in Figure 5.8 and 5.9, both the time over threshold temperature and the melt pool width

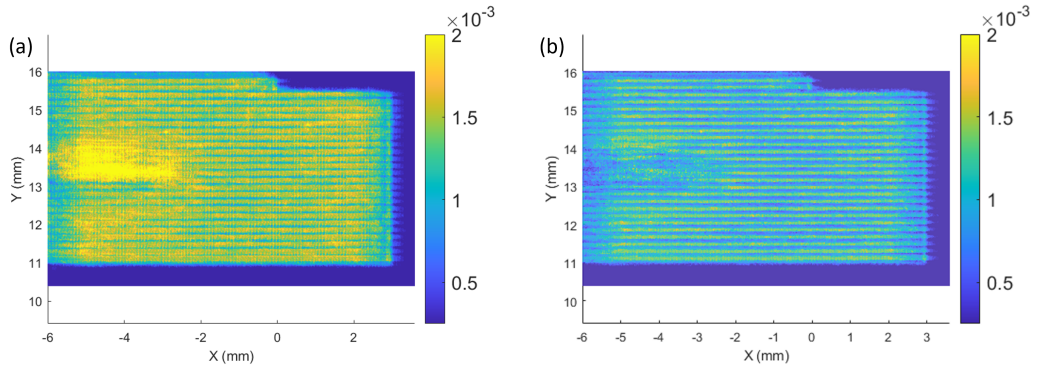

Figure 5.6: (a) The experimental time over threshold in second with threshold = 9. (b) The time over threshold in second with threshold = 15.

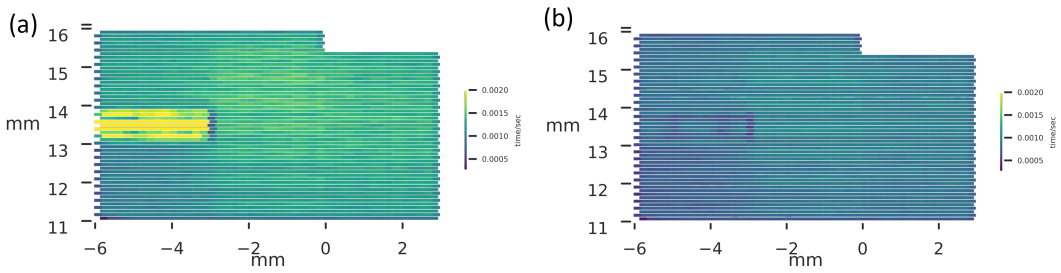

Figure 5.7: (a) The simulation time over threshold in second with threshold = 1290°C. (b) The simulation time over threshold in second with threshold = 1320°C.

display a decreasing trend with layer accumulation. I attributed this phenomenon to the prolonged recoating process in my dataset, which effectively prevents substantial interlayer heat accumulation. Consequently, the primary determinant of temperature distribution is the bottom layers. The platform's low conductivity with the ground (compared with the upper layers which are surrounded by more conductive bulk materials) coupled with prolonged heat exposure of the bottom layers contribute to cooler temperatures in layers further from the bottom.

To explore this phenomenon further, I used my proposed approach with layer

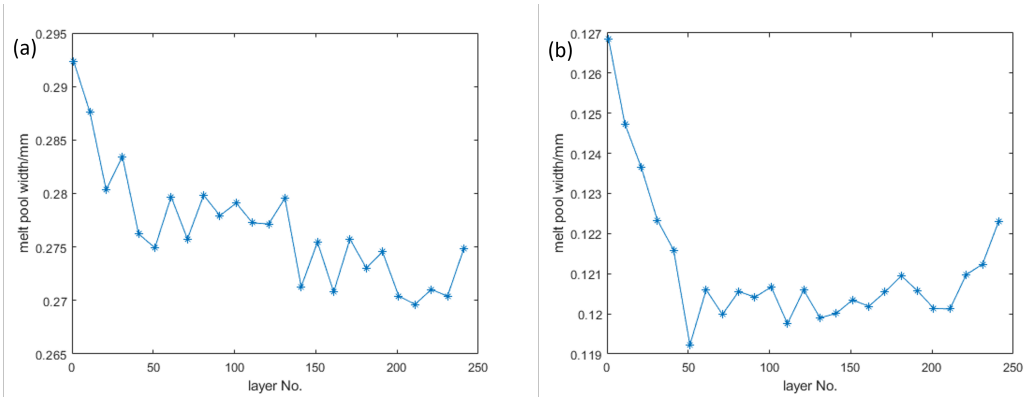

Figure 5.8: (a) Layerwise mean melt pool width with threshold = 7. (b) Layerwise mean melt pool width with threshold = 79.

mode on all layers of the part. The simulation reproduces the expected decreasing trend. Also, the oscillation between layers is captured by the simulation. As shown in Figure 5.9, the time over the threshold in alternating layers from experiments is oscillating. This is because the laser activating time is oscillating by alternating layers due to the sweep direction being different and the changing hatch space in each layer, see Figure 5.10.

While this methodology yields the expected trend, it assumes uniform cooling and heating across the layer, which presents challenges in specific scenarios, such as in overhang regions. As depicted in Figure 5.11, an overestimation of temperature is observed in the overhang region, leading to a notable spike in Figure 5.9. This numerical experiment also demonstrates the integration of both path-level and layer-level approaches is advantageous for a comprehensive analysis.

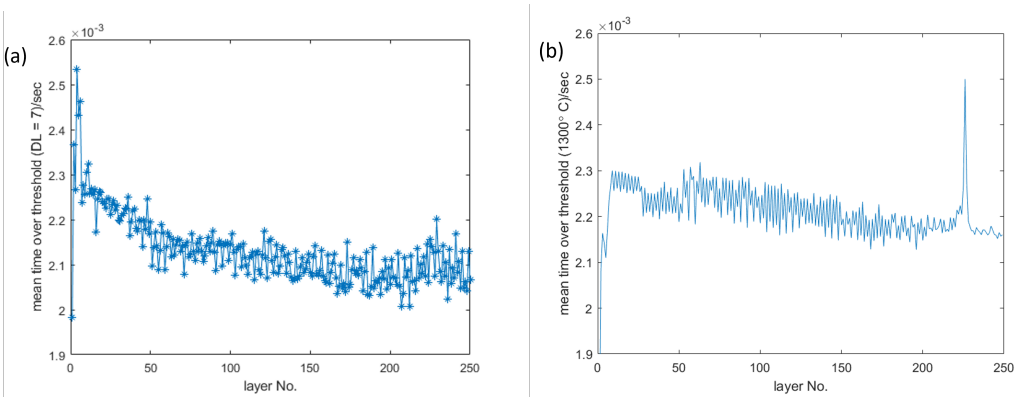

Figure 5.9: (a) The layerwise average time over threshold from experimental data with threshold = 7. (b) Simulation layerwise average time over threshold with the threshold 1300° C (b).

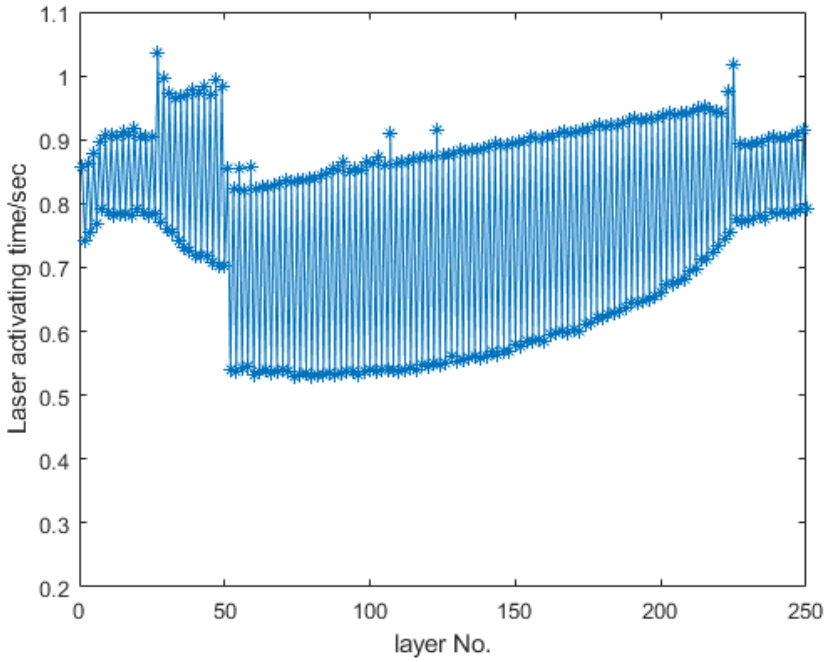

Figure 5.10: The laser activation time of each layer in seconds.

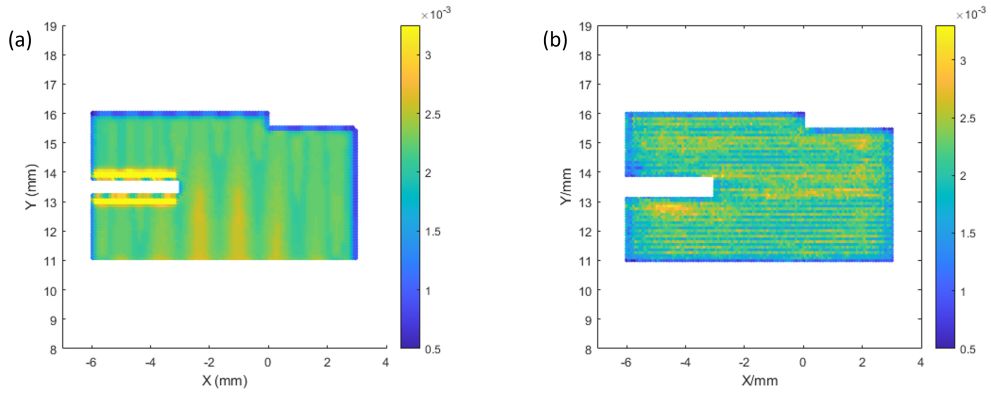

Figure 5.11: The layer-level simulation time over the threshold $(1300°C)$ in second at layer 224. (b) The experimental time over the threshold in second.

5.4 Discussion

In this chapter, I introduced a hybrid layer-path approach to simulate the thermal history of LPBF. This novel approach integrates both path-level and layer-level methodologies, allowing us to accurately access path-level thermal history while maintaining the efficiency of layer-level methods. I investigated the thermal history of a 3D overhang structure fabricated via LPBF using IN625 metal powder with this new approach. Melt pool images captured with the co-axial melt pool monitoring system at NIST were used for calibration and comparison.

By comparing experimental data with simulation results, I observed differences in the time over threshold temperature between the overhang and non-overhang regions in both datasets. I found that the overhang region exhibited a longer time over threshold when the threshold was below the melting point but a shorter time over threshold when the threshold was above the melting point.

Given the capability of the proposed layer-path approach to efficiently capture

thermal history at the path level, it will be advantageous to use the proposed approach in circumstances like feedforward laser power control to enhance part quality. Compared to the layer-level approach, the path-level simulation can capture how the variance of the laser power and the scanning path affect the part quality. The integration of the path-level methodology and the layer-level methodology allows for swift simulations, focusing on regions of interest with path-level simulations to design and optimize intra-layer scanning paths and power.

6 CONCLUSION AND OPEN ISSUES

6.1 Conclusion

In this thesis, I proposed a multiscale thermomechanical simulation framework for the laser powder bed fusion (LPBF) process. This framework includes a path-level thermomechanical simulation that utilizes the path-level thermal history without resolving the detailed melt pool dynamics. The simulated melt pool length shows a 10% relative error compared to experimental data. The path-level residual stress is reproduced with only 1/45 of the elements needed compared to the same problem from the literature. The proposed framework synergistically integrates path-level and layer-level approaches, making the simulation efficient while capturing the effects of the scanning path. Specifically, the framework maintains good efficiency with a low-fidelity approach when far from critical regions. As the simulation approaches critical regions, it switches from lower fidelity to higher fidelity approaches. A good agreement between the experimental and simulated time over threshold on part-scale overhang structures is achieved.

The capability to perform fast thermal or thermomechanical simulations is key for the broader application of the LPBF process. Despite its high design freedom, LPBF is still limited in application due to the slow progress in design automation and pre-qualification of manufactured parts, which is mainly due to the expensive computational cost of LPBF simulation. Conventionally, simulation on the path-level thermomechanical LPBF process on the part-scale problems is still not available. The proposed framework provides the path-level simulation approach, which is validated

against experimental data and simulation results from the literature, providing a more efficient solution compared to the conventional voxel-based approaches. The integration of path-layer approaches further enables the path-level simulation of the part-scale problems.

6.2 Future research

LPBF is a highly localized physical process. Quantifying this localization is crucial for future studies aimed at efficient simulation or process parameter optimization. Traditionally, the high computational expense of LPBF simulation has been attributed to complex multiphysics and the need for fine spatial and temporal discretization. However, this problem might be simpler, and costs could be reduced if correct assumptions are made. Given the localized nature of LPBF, we may not need to simulate large problems with many elements. Instead, solving localized problems might suffice without losing much accuracy: thermal simulations involve the rapid dissipation of heat around the laser, and plasticity mainly occurs around the melt pool regions. Nevertheless, the effects of heat accumulation and global mechanical issues must still be considered. Quantifying localization remains an important issue for future studies. This localization could potentially lead to a model that relates thermal and mechanical responses to a few local process parameters. For example, melt pool shape and inherent strain are related to laser power and speed. Given the constant laser power and speed in practical cases, it is possible to use simplified relations to reduce computational costs. This approach requires an understanding of how to quantify the localized problem, necessitating further research in this area.

Another potential future research direction could be parallel multi-fidelity LPBF simulation. In the present work, the integration of the layer-level approach and the path-level approach is in series: critical regions must be determined in advance, and the path-level simulation relies on the layer-level simulation up to the location near the critical region. A parallel multi-fidelity LPBF simulation could be beneficial: a low-fidelity simulation could be run first, eliminating the need to determine critical regions in advance. All fine-fidelity simulations could then be run in parallel based on the coarse-fidelity simulation results. Currently, I am working on such a parallel path-island-layer multi-fidelity approach.

A APPENDIX

A.1 List of Publications

- Xin Liu, Xingchen Liu, Neel Goldy Kumar, and Paul Witherell. "Scalable path level thermal history simulation of powder bed fusion process validated by melt pool images." Additive Manufacturing 84 (2024): 104111.
- Hongrui Chen, Xin Liu, Xingchen Liu, and Paul Witherell. "MeltpoolGAN: Melt pool prediction from path-level thermal history." Additive Manufacturing 84 (2024): 104095.
- Xin Liu, Xingchen Liu, and Paul Witherell. "A Framework for Simulating the Path-level Residual Stress in the Laser Powder Bed Fusion Process." arXiv preprint arXiv:2407.06293 (2024).
- Xin Liu, Xingchen Liu, Paul Witherell, and Ho Yeung. "An investigation of the Thermal History of Overhang Features in Laser Powder Bed Fusion using a Hybrid Layer-Path Approach." In International Design Engineering Technical Conferences and Computers and Information in Engineering Conference 2024 (accepted).

REFERENCES

[1] Yiğit M Arısoy, Luis E Criales, and Tuğrul Özel. Modeling and simulation of thermal field and solidification in laser powder bed fusion of nickel alloy in625. *Optics & Laser Technology*, 109:278–292, 2019.

[2] L Parry, IA Ashcroft, and Ricky D Wildman. Understanding the effect of laser scan strategy on residual stress in selective laser melting through thermo-mechanical simulation. *Additive Manufacturing*, 12:1–15, 2016.

[3] Brian J Simonds, Jeffrey Sowards, Josh Hadler, Erik Pfeif, Boris Wilthan, Jack Tanner, Chandler Harris, Paul Williams, and John Lehman. Time-resolved absorptance and melt pool dynamics during intense laser irradiation of a metal. *Physical review applied*, 10(4):044061, 2018.

[4] Kaufui V Wong and Aldo Hernandez. A review of additive manufacturing. *International scholarly research notices*, 2012(1):208760, 2012.

[5] Silvia Vock, Burghardt Klöden, Alexander Kirchner, Thomas Weißgärber, and Bernd Kieback. Powders for powder bed fusion: a review. *Progress in Additive Manufacturing*, 4(4):383–397, 2019.

[6] Valmik Bhavar, Prakash Kattire, Vinaykumar Patil, Shreyans Khot, Kiran Gujar, and Rajkumar Singh. A review on powder bed fusion technology of metal additive manufacturing. *Additive manufacturing handbook*, pages 251–253, 2017.

[7] D Dev Singh, T Mahender, and Avala Raji Reddy. Powder bed fusion process: A brief review. *Materials Today: Proceedings*, 46:350–355, 2021.

[8] Wayne E King, Andrew T Anderson, Robert M Ferencz, Neil E Hodge, Chandrika Kamath, Saad A Khairallah, and Alexander M Rubenchik. Laser powder bed fusion additive manufacturing of metals; physics, computational, and materials challenges. *Applied Physics Reviews*, 2(4), 2015.

[9] Pavel Krakhmalev, Gunnel Fredriksson, Krister Svensson, Igor Yadroitsev, Ina Yadroitsava, Mattias Thuvander, and Ru Peng. Microstructure, solidification texture, and thermal stability of 316 l stainless steel manufactured by laser powder bed fusion. *Metals*, 8(8):643, 2018.

[10] Zhihua Tian, Chaoqun Zhang, Dayong Wang, Wen Liu, Xiaoying Fang, Daniel Wellmann, Yongtao Zhao, and Yingtao Tian. A review on laser powder bed fusion of inconel 625 nickel-based alloy. *Applied Sciences*, 10(1):81, 2019.

[11] Sheng Cao, Yichao Zou, Chao Voon Samuel Lim, and Xinhua Wu. Review of laser powder bed fusion (lpbf) fabricated ti-6al-4v: process, post-process treatment, microstructure, and property. *Light: Advanced Manufacturing*, 2(3):313–332, 2021.

[12] Vaishnav Madhavadas, Divyansh Srivastava, Utkarsh Chadha, Sakthivel Aravind Raj, Mohamed Thariq Hameed Sultan, Farah Syazwani Shahar, and Ain Umaira Md Shah. A review on metal additive manufacturing for intricately shaped aerospace components. *CIRP Journal of Manufacturing Science and Technology*, 39:18–36, 2022.

[13] Elena Bassoli, Silvio Defanti, Emanuele Tognoli, Nicolò Vincenzi, and Lorenzo

Degli Esposti. Design for additive manufacturing and for machining in the automotive field. *Applied Sciences*, 11(16):7559, 2021.

[14] Keyvan Safaei, Hossein Abedi, Mohammadreza Nematollahi, Fatemeh Kordizadeh, Hediyeh Dabbaghi, Parisa Bayati, Reza Javanbakht, Ahmadreza Jahadakbar, Mohammad Elahinia, and Behrang Poorganji. Additive manufacturing of niti shape memory alloy for biomedical applications: review of the lpbf process ecosystem. *Jom*, pages 1–16, 2021.

[15] Ranadip Acharya, John A Sharon, and Alexander Staroselsky. Prediction of microstructure in laser powder bed fusion process. *Acta Materialia*, 124:360–371, 2017.

[16] Alexandra Hilaire, Eric Andrieu, and Xinhua Wu. High-temperature mechanical properties of alloy 718 produced by laser powder bed fusion with different processing parameters. *Additive Manufacturing*, 26:147–160, 2019.

[17] K Inaekyan, A Kreitcberg, S Turenne, and V Brailovski. Microstructure and mechanical properties of laser powder bed-fused in625 alloy. *Materials Science and Engineering: A*, 768:138481, 2019.

[18] Sohini Chowdhury, N Yadaiah, Chander Prakash, Seeram Ramakrishna, Saurav Dixit, Lovi Raj Gupta, and Dharam Buddhi. Laser powder bed fusion: a state-of-the-art review of the technology, materials, properties & defects, and numerical modelling. *Journal of Materials Research and Technology*, 20:2109–2172, 2022.

[19] M Reza Yavari, Kevin D Cole, and Prahalada Rao. Thermal modeling in metal additive manufacturing using graph theory. *Journal of Manufacturing Science and Engineering*, 141(7), 2019.

[20] Zhi-Jian Li, Hong-Liang Dai, Yuan Yao, and Jin-Ling Liu. A semi-analytical model for rapid prediction of residual stress and deformation in laser powder bed fusion. *Applied Mathematical Modelling*, 125:672–686, 2024.

[21] William H Gourdin. Dynamic consolidation of metal powders. *Progress in Materials Science*, 30(1):39–80, 1986.

[22] Alexis Queva, Gildas Guillemot, Clara Moriconi, Charlotte Metton, and Michel Bellet. Numerical study of the impact of vaporisation on melt pool dynamics in laser powder bed fusion-application to in718 and ti–6al–4v. *Additive Manufacturing*, 35:101249, 2020.

[23] Prveen Bidare, Ioannis Bitharas, RM Ward, MM Attallah, and Andrew J Moore. Fluid and particle dynamics in laser powder bed fusion. *Acta Materialia*, 142:107–120, 2018.

[24] Manyalibo J Matthews, Gabe Guss, Saad A Khairallah, Alexander M Rubenchik, Philip J Depond, and Wayne E King. Denudation of metal powder layers in laser powder-bed fusion processes. In *Additive Manufacturing Handbook*, pages 677–692. CRC Press, 2017.

[25] John G Michopoulos, Athanasios P Iliopoulos, John C Steuben, Andrew J Birnbaum, and Samuel G Lambrakos. On the multiphysics modeling challenges for

metal additive manufacturing processes. *Additive Manufacturing*, 22:784–799, 2018.

[26] Christof Lüthi, Mamzi Afrasiabi, and Markus Bambach. An adaptive smoothed particle hydrodynamics (sph) scheme for efficient melt pool simulations in additive manufacturing. *Computers & Mathematics with Applications*, 139:7–27, 2023.

[27] Tesfaye Moges, Gaurav Ameta, and Paul Witherell. A review of model inaccuracy and parameter uncertainty in laser powder bed fusion models and simulations. *Journal of manufacturing science and engineering*, 141(4):040801, 2019.

[28] Rishi K Ganeriwala, Neil E Hodge, and Jerome M Solberg. Towards improved speed and accuracy of laser powder bed fusion simulations via multiscale spatial representations. *Computational Materials Science*, 187:110112, 2021.

[29] Zhibo Luo and Yaoyao Zhao. A survey of finite element analysis of temperature and thermal stress fields in powder bed fusion additive manufacturing. *Additive Manufacturing*, 21:318–332, 2018.

[30] Yang Cao, Xin Lin, Nan Kang, Liang Ma, Lei Wei, Min Zheng, Jun Yu, Dongjian Peng, and Weidong Huang. A novel high-efficient finite element analysis method of powder bed fusion additive manufacturing. *Additive Manufacturing*, 46:102187, 2021.

[31] Yangzhan Yang, Madie Allen, Tyler London, and Victor Oancea. Residual strain predictions for a powder bed fusion inconel 625 single cantilever part. *Integrating Materials and Manufacturing Innovation*, 8(3):294–304, 2019.

[32] Erik R Denlinger, Jarred C Heigel, and Panagiotis Michaleris. Residual stress and distortion modeling of electron beam direct manufacturing ti-6al-4v. *Proceedings of the Institution of Mechanical Engineers, Part B: Journal of Engineering Manufacture*, 229(10):1803–1813, 2015.

[33] Erik R Denlinger, Michael Gouge, Jeff Irwin, and Pan Michaleris. Thermomechanical model development and in situ experimental validation of the laser powder-bed fusion process. *Additive Manufacturing*, 16:73–80, 2017.

[34] MC Sow, Thibaut De Terris, Olivier Castelnau, Z Hamouche, Frédéric Coste, Rémy Fabbro, and Patrice Peyre. Influence of beam diameter on laser powder bed fusion (l-pbf) process. *Additive Manufacturing*, 36:101532, 2020.

[35] Jonas Grünewald, Florian Gehringer, Maximilian Schmöller, and Katrin Wudy. Influence of ring-shaped beam profiles on process stability and productivity in laser-based powder bed fusion of aisi 316l. *Metals*, 11(12):1989, 2021.

[36] Wentao Yan, Jacob Smith, Wenjun Ge, Feng Lin, and Wing Kam Liu. Multiscale modeling of electron beam and substrate interaction: a new heat source model. *Computational Mechanics*, 56(2):265–276, 2015.

[37] Alexander J Dunbar, Erik R Denlinger, Michael F Gouge, and Pan Michaleris. Experimental validation of finite element modeling for laser powder bed fusion deformation. *Additive Manufacturing*, 12:108–120, 2016.

[38] Jiangwei Liu, Guichuan Li, Qidong Sun, Hu Li, Jie Sun, and Xiebin Wang. Understanding the effect of scanning strategies on the microstructure and crys-

tallographic texture of ti-6al-4v alloy manufactured by laser powder bed fusion. *Journal of Materials Processing Technology*, 299:117366, 2022.

[39] Naresh Nadammal, Tatiana Mishurova, Tobias Fritsch, Itziar Serrano-Munoz, Arne Kromm, Christoph Haberland, Pedro Dolabella Portella, and Giovanni Bruno. Critical role of scan strategies on the development of microstructure, texture, and residual stresses during laser powder bed fusion additive manufacturing. *Additive Manufacturing*, 38:101792, 2021.

[40] Changpeng Chen, Zhongxu Xiao, Yilong Wang, Xu Yang, and Haihong Zhu. Prediction study on in-situ reduction of thermal stress using combined laser beams in laser powder bed fusion. *Additive Manufacturing*, 47:102221, 2021.

[41] Nachiket Patil, Rishi Ganeriwala, Jerome M Solberg, Neil E Hodge, and Robert M Ferencz. Benchmark multi-layer simulations for residual stresses and deformation in small additively manufactured metal parts. *Additive Manufacturing*, 45:102015, 2021.

[42] Hao Peng, Morteza Ghasri-Khouzani, Shan Gong, Ross Attardo, Pierre Ostiguy, Ronald B Rogge, Bernice Aboud Gatrell, Joseph Budzinski, Charles Tomonto, Joel Neidig, et al. Fast prediction of thermal distortion in metal powder bed fusion additive manufacturing: Part 2, a quasi-static thermo-mechanical model. *Additive Manufacturing*, 22:869–882, 2018.

[43] Michael F Zaeh and Gregor Branner. Investigations on residual stresses and deformations in selective laser melting. *Production Engineering*, 4(1):35–45, 2010.

[44] P Prabhakar, William J Sames, R Dehoff, and Sudarsanam Suresh Babu. Computational modeling of residual stress formation during the electron beam melting process for inconel 718. *Additive Manufacturing*, 7:83–91, 2015.

[45] Wenyou Zhang, Mingming Tong, and Noel M Harrison. Resolution, energy and time dependency on layer scaling in finite element modelling of laser beam powder bed fusion additive manufacturing. *Additive Manufacturing*, 28:610–620, 2019.

[46] Mohamad Bayat, Christopher G Klingaa, Sankhya Mohanty, David De Baere, Jesper Thorborg, Niels S Tiedje, and Jesper H Hattel. Part-scale thermo-mechanical modelling of distortions in laser powder bed fusion–analysis of the sequential flash heating method with experimental validation. *Additive Manufacturing*, 36:101508, 2020.

[47] Matteo Bugatti and Quirico Semeraro. Limitations of the inherent strain method in simulating powder bed fusion processes. *Additive Manufacturing*, 23:329–346, 2018.

[48] Xuan Liang, Lin Cheng, Qian Chen, Qingcheng Yang, and Albert C To. A modified method for estimating inherent strains from detailed process simulation for fast residual distortion prediction of single-walled structures fabricated by directed energy deposition. *Additive Manufacturing*, 23:471–486, 2018.

[49] Xuan Liang, Wen Dong, Qian Chen, and Albert C To. On incorporating scanning strategy effects into the modified inherent strain modeling framework for laser powder bed fusion. *Additive Manufacturing*, 37:101648, 2021.

[50] Yukio Ueda, Keiji Fukuda, and Masayuki Tanigawa. New measuring method of three dimensional residual stresses based on theory of inherent strain (welding mechanics, strength & design). *Transactions of JWRI*, 8(2):249–256, 1979.

[51] Xingchen Liu and Vadim Shapiro. Homogenization of material properties in additively manufactured structures. *Computer-Aided Design*, 78:71–82, 2016.

[52] Michael Gouge, Erik Denlinger, Jeff Irwin, Chao Li, and Pan Michaleris. Experimental validation of thermo-mechanical part-scale modeling for laser powder bed fusion processes. *Additive Manufacturing*, 29:100771, 2019.

[53] Yaqi Zhang and Vadim Shapiro. Linear-time thermal simulation of as-manufactured fused deposition modeling components. *Journal of Manufacturing Science and Engineering*, 140(7), 2018.

[54] Yaqi Zhang, Vadim Shapiro, and Paul Witherell. Towards thermal simulation of powder bed fusion on path level. In *International Design Engineering Technical Conferences and Computers and Information in Engineering Conference*, volume 59179, page V001T02A034. American Society of Mechanical Engineers, 2019.

[55] Yaqi Zhang, Vadim Shapiro, and Paul Witherell. A scalable framework for process-aware thermal simulation of additive manufacturing processes. *Journal of Computing and Information Science in Engineering*, 22(1), 2022.

[56] Brandon Lane, Sergey Mekhontsev, Steven Grantham, ML Vlasea, Justin Whiting, Ho Yeung, Jason Fox, Clarence Zarobila, Jorge Neira, Michael McGlauflin, et al. Design, developments, and results from the nist additive manufactur-

ing metrology testbed (ammt). In *2016 International Solid Freeform Fabrication Symposium*. University of Texas at Austin, 2016.

[57] Ho Yeung and Brandon Lane. A residual heat compensation based scan strategy for powder bed fusion additive manufacturing. *Manufacturing letters*, 25:56–59, 2020.

[58] Yaqi Zhang. *A Scalable Framework for Contact-Aware Thermal Simulation of Additive Manufacturing Processes*. The University of Wisconsin-Madison, 2020.

[59] Johannes Trapp, Alexander M Rubenchik, Gabe Guss, and Manyalibo J Matthews. In situ absorptivity measurements of metallic powders during laser powder-bed fusion additive manufacturing. *Applied Materials Today*, 9:341–349, 2017.

[60] Manyalibo Matthews, Johannes Trapp, Gabe Guss, and Alexander Rubenchik. Direct measurements of laser absorptivity during metal melt pool formation associated with powder bed fusion additive manufacturing processes. *Journal of Laser Applications*, 30(3):032302, 2018.

[61] Brandon Lane, Ivan Zhirnov, Sergey Mekhontsev, Steven Grantham, Richard Ricker, Santosh Rauniyar, and Kevin Chou. Transient laser energy absorption, coaxial melt pool monitoring, and relationship to melt pool morphology. *Additive Manufacturing*, 36:101504, 2020.

[62] Yaasin A Mayi, Morgan Dal, Patrice Peyre, Michel Bellet, Charlotte Metton, Clara Moriconi, and Remy Fabbro. Transient dynamics and stability of keyhole

at threshold in laser powder bed fusion regime investigated by finite element modeling. *Journal of Laser Applications*, 33(1):012024, 2021.

[63] Hui Huang, Yiyu Wang, Jian Chen, and Zhili Feng. An efficient numerical model for predicting residual stress and strain in parts manufactured by laser powder bed fusion. *Journal of Physics: Materials*, 4(4):044006, 2021.

[64] Chengcheng Wang, XP Tan, SB Tor, and CS Lim. Machine learning in additive manufacturing: State-of-the-art and perspectives. *Additive Manufacturing*, 36:101538, 2020.

[65] Sayyeda Saadia Razvi, Shaw Feng, Anantha Narayanan, Yung-Tsun Tina Lee, and Paul Witherell. A review of machine learning applications in additive manufacturing. In *International Design Engineering Technical Conferences and Computers and Information in Engineering Conference*, volume 59179, page V001T02A040. American Society of Mechanical Engineers, 2019.

[66] Lyle Regenwetter, Amin Heyrani Nobari, and Faez Ahmed. Deep generative models in engineering design: A review. *Journal of Mechanical Design*, 144(7):071704, 2022.

[67] Ian Goodfellow, Jean Pouget-Abadie, Mehdi Mirza, Bing Xu, David Warde-Farley, Sherjil Ozair, Aaron Courville, and Yoshua Bengio. Generative adversarial networks. *Communications of the ACM*, 63(11):139–144, 2020.

[68] Phillip Isola, Jun-Yan Zhu, Tinghui Zhou, and Alexei A Efros. Image-to-image translation with conditional adversarial networks. In *Proceedings of the IEEE conference on computer vision and pattern recognition*, pages 1125–1134, 2017.

[69] Hongrui Chen and Xingchen Liu. Geometry enhanced generative adversarial networks for random heterogeneous material representation. In *International Design Engineering Technical Conferences and Computers and Information in Engineering Conference*, volume 85383, page V03AT03A020. American Society of Mechanical Engineers, 2021.

[70] Hongrui Chen, Xin Liu, Xingchen Liu, and Paul Witherell. Meltpoolgan: Melt pool prediction from path-level thermal history. *Additive Manufacturing*, 84:104095, 2024.

[71] Xin Liu, Xingchen Liu, Neel Goldy Kumar, and Paul Witherell. Scalable path level thermal history simulation of powder bed fusion process validated by melt pool images. *Additive Manufacturing*, page 104111, 2024.

[72] Changpeng Chen, Jie Yin, Haihong Zhu, Zhongxu Xiao, Luo Zhang, and Xiaoyan Zeng. Effect of overlap rate and pattern on residual stress in selective laser melting. *International Journal of Machine Tools and Manufacture*, 145:103433, 2019.

[73] Wenyou Zhang, Mingming Tong, and Noel M Harrison. Scanning strategies effect on temperature, residual stress and deformation by multi-laser beam powder bed fusion manufacturing. *Additive Manufacturing*, 36:101507, 2020.

[74] Payam Dadvand, Riccardo Rossi, and Eugenio Oñate. An object-oriented environment for developing finite element codes for multi-disciplinary applications. *Arch Computat Methods Eng*, 17:253–297, 2010.

[75] Payam Dadvand, Riccardo Rossi, Mariano Gil, Xavier Martorell, Jordi Cotela, Enric Juanpere, Sergio Idelsohn, and Eugenio Oñate. Migration of a generic

multi-physics framework to hpc environments. *Computers & Fluids*, 80:301–309, 2013.

[76] Vicente Mataix Ferrándiz, Philipp Bucher, Rubén Zorrilla, Riccardo Rossi, Jordi Cotela, Alejandro Cornejo Velázquez, Miguel Angel Celigueta, Josep Maria, Tobias Teschemacher, Carlos Roig, Miguel Maso, Guillermo Casas, Suneth Warnakulasuriya, Marc Núñez, Pooyan Dadvand, Salva Latorre, Ignasi de Pouplana, Joaquín Irazábal González, Ferran Arrufat, and Javi Gárate. KratosMultiphysics/Kratos: Release 9.2 (v9.2). `https://doi.org/10.5281/zenodo.3234644`, 2022.

[77] Jamasp Jhabvala, Eric Boillat, Thibaud Antignac, and Rémy Glardon. On the effect of scanning strategies in the selective laser melting process. *Virtual and physical prototyping*, 5(2):99–109, 2010.

[78] Qian Chen, Hunter Taylor, Akihiro Takezawa, Xuan Liang, Xavier Jimenez, Ryan Wicker, and Albert C To. Island scanning pattern optimization for residual deformation mitigation in laser powder bed fusion via sequential inherent strain method and sensitivity analysis. *Additive Manufacturing*, 46:102116, 2021.

[79] Brandon Lane, Ho Yeung, and Zhuo Yang. Statistical and spatio-temporal data features in melt pool monitoring of additive manufacturing. In *IIE Annual Conference. Proceedings*, pages 1–6. Institute of Industrial and Systems Engineers (IISE), 2022.

[80] Claire Bruna-Rosso, Ali Gökhan Demir, and Barbara Previtali. Selective laser melting finite element modeling: Validation with high-speed imaging and lack of fusion defects prediction. *Materials & Design*, 156:143–153, 2018.

[81] Mohamad Bayat, Aditi Thanki, Sankhya Mohanty, Ann Witvrouw, Shoufeng Yang, Jesper Thorborg, Niels Skat Tiedje, and Jesper Henri Hattel. Keyhole-induced porosities in laser-based powder bed fusion (l-pbf) of ti6al4v: High-fidelity modelling and experimental validation. *Additive Manufacturing*, 30:100835, 2019.

[82] Xin Liu, Xingchen Liu, Neel Goldy Kumar, and Paul Witherell. Scalable path level thermal history simulation of powder bed fusion process validated by melt pool images. *Additive Manufacturing*, 84:104111, 2024.

[83] Brandon Lane and Ho Yeung. Process monitoring dataset from the additive manufacturing metrology testbed (ammt): Overhang part x4. *Journal of Research of the National Institute of Standards and Technology*, 125:1–18, 2020.

[84] F Sakuma. Establishing a practical temperature standard by using a narrow-bannd radiation thermometer with a silicon detector. *Temperature, Its Measurement and Control in Science and Industry*, 5:421–427, 1982.

[85] Zhuo Yang, Yan Lu, Brandon Lane, Jaehyuk Kim, Yande Ndiaye, and Sundar Krishnamruty. Analyzing remelting conditions based on in-situ melt pool data fusion for overhang building in powder bed fusion process. 2021.